

Chapter 2

Tropospheric trace-gas measurements with the differential-absorption lidar technique

Thomas Trickl

*Karlsruher Institut für Technologie, IMK-IFU,
Kreuzeckbahnstr. 19, D-82467 Garmisch-Partenkirchen,
Germany, thomas.trickl@kit.edu*

1. Introduction

Laser-spectroscopic methods have been invaluable tools in laboratory studies of chemical and physical processes. The sensitivity of fluorescence and photo-ionization approaches reaches levels down to single-atom or -molecule detection. Less sensitive methods, such as four-wave-mixing and diode-laser absorption spectrometry, have been applied for trace-gas detection in moderate-pressure gas. For lidar sounding of atmospheric trace constituents a number of restrictions must be considered. Most of the laser methods used in the laboratory cannot be applied in atmospheric lidar studies, and even the laser-induced-fluorescence technique can only yield its full potential in the upper atmosphere (e.g., Refs.1-4) due to collisional fluorescence quenching at lower altitudes.

As a consequence, tropospheric and lower-stratospheric measurements have most commonly been carried out by absorption measurements. Absorption measurements are not influenced by quenching, but are certainly less sensitive than fluorescence and photo-ionization approaches. A non-zero background from Rayleigh and particle backscattering exists, necessitating signal averaging over many thousand laser shots to make a weak specific absorption feature visible in the noise. In order to avoid tuning of the laser frequency across spectral lines two (and more) wavelengths are used for the differential absorption measurements. In the differential-absorption lidar (DIAL) technique one (or more) “on” laser wavelengths are set to specific absorption lines or regions of a trace gas, and the so-called “off” wavelength is selected in a spectral region with low or negligible absorption, creating a reference backscatter signal [5,6]. Overviews of the DIAL method have been

given in several books chapters [7-13]. Details of the method are described in Sec. 2.

DIAL measurements covering at least parts of the free troposphere are limited to wavelengths below 1 μm where sufficiently strong Rayleigh backscattering exists. This means a strong limitation since most molecules absorb at longer wavelengths where their vibrational-rotational transitions are located and where they are most commonly probed with low to moderate vertical resolution by Fourier-transform (FTIR) techniques [14] (see, e.g., Ref. 15 for a sensitivity analysis). Species accessible to DIAL sounding in the visible and ultraviolet (UV) spectral ranges, e.g., are O_3 , H_2O , NO , NH_3 , NO_2 , SO_2 , Cl_2 , ClO , OCIO , Hg and a few hydrocarbons. Air pollution measurements, frequently with three-dimensional scanning lidar systems, have also been made by numerous groups (e.g., Refs. 16-38). Nevertheless, some DIAL measurements have been made in the infrared (IR) with chemical, Raman-shifted and solid-state lasers, as well as optical-parametric oscillators and CO_2 lasers [32, 39-53]. These measurements require the presence of aerosol and are limited to the boundary layer. The sensitivity of the infrared methods, even for dust-loaded atmospheres, significantly decreases with growing wavelength, the maximum wavelength used being roughly 10 μm (CO_2 laser).

However, apart from air-pollution plumes, the ambient concentrations of most molecules that can be probed by the DIAL method are rather low. For instance, the free-tropospheric background NO_2 mixing ratios are of the order of 0.1 ppb (parts per billion as compared with the air number density) which is far below the detection threshold even if one tries to determine the tropospheric column. Also the chemical age is an important factor since well-mixed gases do not exhibit a vertical structure and do not require vertical sounding. As a consequence most efforts have been devoted to vertical sounding of ozone and water vapour. For these two trace constituents many detailed studies of the atmospheric processes underlying their vertical distributions and routine measurements have been carried out. In this section, we focus on measurements also covering at least parts of the free troposphere, which limits the discussion mostly to the ozone and the water-vapour DIAL.

Ozone and water vapour represent two extreme cases of DIAL measurements. Water vapour may be seen as a classical DIAL species because of the existence of discrete spectral lines, whereas the ultraviolet (UV) absorption spectrum of ozone does not exhibit any narrow-band structure necessitating a significant separation of the “on” and the “off” wavelengths.

The tropospheric ozone DIAL, in the most commonly used versions, has emerged from the approach used in stratospheric systems (e.g., [54-55]). The light absorption of ozone in the Hartley-Huggins UV band systems (wavelengths less than 320 nm, see Fig. 1) has been used. The monitoring of stratospheric ozone with DIAL is a mature and proven approach and has been applied world wide, in particular within the Network of the Detection of Atmospheric Composition Change (NDACC, <http://www.ndsc.ncep.noaa.gov/>). DIAL sounding of tropospheric ozone is substantially more demanding due to the presence of aerosol, clouds and, in polluted areas, other trace gases that also absorb light in the same wavelength region, such as SO₂ and NO₂. Furthermore, for systems covering both the boundary layer and the free troposphere, the dynamic range of the backscatter signal exceeds that in stratospheric systems by many decades, an enormous task for the receiver layout and the detection electronics. A large number of tropospheric ozone DIAL systems have been developed for stationary, mobile and air-borne applications (e.g., [56-87]). In Europe even an international research project, TESLAS (Tropospheric Environmental Studies by Laser Sounding, 1988-1996), focussed on the development of ozone DIAL systems [88]. Despite reasonable initial support and the high technical standard reached, the operation of tropospheric DIAL systems has remained rather limited world wide. An important limiting factor has been the considerable costs of the DIAL technology.

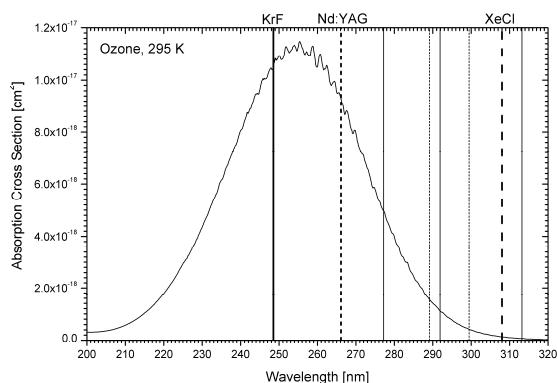


Fig. 1. Absorption cross sections of ozone for 295 K [133,134]; the vertical lines show three frequently used fixed-frequency laser wavelengths (KrF laser, frequency-quadrupled Nd:YAG laser, and XeCl laser) together with the wavelengths for first- and second-Stokes shifted emissions for Raman-shifting in H₂ and D₂.

Water vapour DIAL systems have been operated in the near IR mostly in the band systems between 700 and 950 nm (see Fig. 2) and have also been developed for ground-based and air-borne measurements (e.g., [5, 13, 89-115]). Lidar sounding of water vapour is a true challenge, for both DIAL and Raman lidar systems. This is a consequence of the drop in water-vapour density by about four decades from the ground into the stratosphere and, at the same time, the strong drop of the lidar return as a function of distance. The situation is less problematic for air-borne DIAL systems. Here, the concentration grows with distance. A demanding laser technique is required involving spectrally pure stabilized tunable laser systems, a considerable task for shaky air-borne systems [13]. Although stand-alone operation of a DIAL system around the clock and throughout the year has been demonstrated [116] the advanced narrow-band laser technique required for water-vapour sounding is to some extent seen as a disadvantage leading to some preference for the Raman lidar approach. The method is, nevertheless, highly attractive because of the high temporal and vertical resolution, the excellent daytime capability even up to high altitudes [113] as well as the intrinsic calibration stability of a DIAL (see Sec. 2.1).

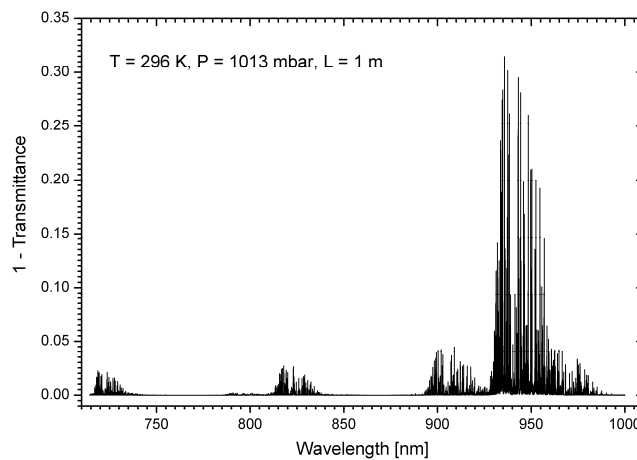


Fig. 2. Near-IR spectrum for light transmitted through 1 m of air with 10 % water vapour, at 295 K and 1013 mbar, showing the three absorption bands of water vapour most frequently used for DIAL measurements (around 718 nm, 817 nm and 935 nm). The spectrum was calculated with the MOLSPEC 2.2.1 program (Laser Components) based on listings from the HITRAN 2000 data base [141].

Despite the limited use, DIAL systems have yielded a considerable contribution to atmospheric research otherwise difficult to obtain. Different approaches have been followed. Air-borne systems may actively search and map atmospheric layers in three dimensions, an invaluable approach in atmospheric transport studies. These lidar measurements can be combined with sensitive on-board *in-situ* measurements during aircraft ascents and descents through specific layers that add the complementary information on trace gases not accessible to optical remote sensing. In this way, the chemical composition and transformation of air masses may be studied. Ground based systems probe the atmospheric layers by extended time series, taking benefit from the transport of the respective air masses across the observational area for gaining some spatial information. One advantage of ground-based lidar measurements is a usually better vertical resolution due to the missing limitation of the averaging times imposed by the motion of an aeroplane. Another advantage is the possibility of long-term measurements and trend studies, which is problematic for air-borne systems due to the high costs of the flight missions.

2. The differential-absorption method

2.1 General expressions

The DIAL method is, in principle, designed for an application to atmospheric constituents with a well resolved line spectrum. This allows one to select laser frequencies distant by just a few Gigahertz and, therefore, to eliminate to a major extent the influence of processes with small wavelength dependence such as backscattering of radiation by aerosols. The most prominent absorber of this kind is water vapour. The vibrational-rotational spectrum of water vapour extends to the near-infrared spectral range where sufficient Rayleigh backscattering for free-tropospheric measurements exists. The most commonly used bands are located around 725, 817 and 935 nm (see Fig. 2 for an example). Another example of a molecule with partly well-resolved spectrum is NO for which the strong electronic $A^2\Sigma^+ - X^2\Pi$ transition (“Gamma Bands”) around 227 nm is used [17,26]. One disadvantage for lidar measurements in this wavelength region is the considerable signal loss due to light absorption by oxygen and ozone and by Rayleigh scattering. For other molecular species, such as SO₂ and NO₂, the energy levels are too dense under atmospheric conditions for single-line

distinction. Differential absorption with two still rather closely-spaced laser wavelengths can be obtained in the vicinity of band heads.

The UV spectrum of ozone is broadened due to fast photo-decomposition [117]. Here, a rather large gap between the laser wavelengths is necessary (Fig. 1). For stratospheric measurements, most commonly, the emission of a xenon-chloride laser at 308 nm is used [55,118]. In fact, 308 nm is the optimum “on” wavelength for reaching high altitudes in the stratosphere (50 km and more). In the troposphere the ozone density is much lower. For tropospheric measurements, therefore, shorter “on” wavelengths, down to the wavelength of the frequency-quadrupled Nd:YAG laser (266.1 nm) have been used. For the “off” wavelengths of ozone DIALs, in most systems a part of the laser emission is partially shifted by stimulated Raman scattering (see selected papers from the list cited in the Introduction [56-88], and [119-125]). For tropospheric ozone DIAL systems the simultaneous use of at least three wavelengths is, meanwhile, state of the art. This yields two and more separate ozone profiles with different useful ranges and results in an internal quality control.

In the following, the basics of the DIAL algorithms are described. We start from the lidar equations for the power P received from a range bin Δr for the two wavelengths λ_{on} and λ_{off} :

$$P_i(r) = P_i(\lambda_i) \kappa_L(\lambda_i) \frac{O_i(r) A \Delta r}{r^2} \beta(r, \lambda_i) t_{\uparrow}(r, \lambda_i) t_{\downarrow}(r, \lambda_i), \quad i = \text{“on” or “off”}, \quad (1)$$

with the backscatter coefficient $\beta = \beta_R + \beta_P$ (R for “Rayleigh”, P for “particles”) the system sensitivity constant κ , the overlap function O , the receiver area A and the transmittances t_{\uparrow} and t_{\downarrow} for the upward and downward going light, respectively. As will be explained further below, t_{\uparrow} and t_{\downarrow} are slightly different in the case of molecules with well-resolved lines such as H_2O , the factorization being an approximation for narrow-band laser emission. Otherwise, the application of Beer and Lambert’s law yields

$$t_{\uparrow}(r, \lambda_i) t_{\downarrow}(r, \lambda_i) = \exp\left(-2 \int_0^r \alpha(\lambda_i, r') dr'\right), \quad (2)$$

with the extinction coefficient $\alpha_R + \alpha_P + \alpha_M + \alpha_A$ (M for the absorption by the molecule under investigation, A for the sum of the other absorption losses). After derivative formation, one obtains from the two Eqs. 1

$$\frac{d}{dr} \ln\left(\frac{P(\lambda_{on}, r)}{P(\lambda_{off}, r)}\right) = \frac{d}{dr} \ln\left(\frac{\beta(\lambda_{on}, r)}{\beta(\lambda_{off}, r)}\right) - 2(\alpha(\lambda_{on}, r) - \alpha(\lambda_{off}, r)). \quad (3)$$

This equation is then converted to

$$\begin{aligned}
 n_M(r) = & -[2(\sigma_M(\lambda_{on}, r) - \sigma_M(\lambda_{off}, r))]^{-1} \left\{ \frac{d}{dr} \ln\left(\frac{P(\lambda_{on}, r)}{P(\lambda_{off}, r)}\right) + \text{ (“DIAL equation”)} \right. \\
 & + \frac{d}{dr} \ln\left(\frac{\beta(\lambda_{on}, r)}{\beta(\lambda_{off}, r)}\right) - \text{ (“backscatter term”)} \\
 & \left. - 2[(\alpha_R(\lambda_{on}, r) - \alpha_R(\lambda_{off}, r)) + (\alpha_P(\lambda_{on}, r) - \alpha_P(\lambda_{off}, r)) + (\alpha_A(\lambda_{on}, r) - \alpha_A(\lambda_{off}, r))] \right\}, \\
 & \text{ (“extinction term”)}
 \end{aligned}$$

$n_M(r)$ being the number density of species M and $\sigma_M(\lambda, r)$ its absorption cross section (which changes as a function of the temperature, i.e., the altitude). The first line represents the so-called “DIAL equation”. It is obvious that, under conditions when the correction terms described in lines 2 – 3 of Eq. 4 are negligible, the accuracy of the DIAL method is just determined by that of the absorption cross sections and the quality of the backscatter signals P. This makes the method very valuable for long-term investigations in the free troposphere and in the stratosphere.

For molecules with a dense spectrum the backscatter and extinction terms do not matter, if the distance between “on” and “off” wavelengths are short. For ozone, this is not the case (see Introduction). Here, in particular the backscatter term matters in the presence of steep aerosol gradients and must be carefully corrected. The most commonly used methods are described in Sec. 2.4. The errors due to differential extinction in an ozone DIAL are usually small. Both the impact of aerosols and molecular species must be considered, mostly in the boundary layer. The most important trace gases interfering in the wavelength region relevant for tropospheric ozone measurements (266 nm to 313 nm) are NO₂ and SO₂. Some hydrocarbons might also matter, but there is not much information on this in the literature. In the free troposphere the interference by differential molecular absorption is negligible.

For a molecule with well-separated absorption lines as H₂O, both the lidar and the DIAL equations are just approximations, due to the Rayleigh-Brillouin broadening of the backscattered light [126, 127]. Its bandwidth becomes comparable with the atmospheric absorption line width of H₂O. As a consequence, the light absorption is slightly modified on the downward path, leading to different absorption cross sections σ_{\uparrow} and σ_{\downarrow} for the upward and downward propagation of the light [128]. This effect is rather small in the case of pure Rayleigh scattering or even negligible for clearly

dominating light scattering by aerosols. In the mixed case deviations of more than 20 % may be reached in vertical sections with significant aerosol gradients. More information is found in Sec. 2.4.

The method is described in detail by Bösenberg [129]. The modified DIAL equation may be written for the H₂O number density as:

$$n_{H_2O}(r) = \frac{1}{\Delta\sigma_{\uparrow}(r) + \Delta\sigma_{\downarrow}(r)} \left(G(\lambda_{on}, r) - \frac{d}{dr} \ln \left(\frac{P(\lambda_{on}, r)}{P(\lambda_{off}, r)} \right) \right), \quad (5)$$

with $\Delta\sigma_{\uparrow\downarrow}(r) = \sigma_{H_2O, \uparrow\downarrow}(\lambda_{on}, r) - \sigma_{H_2O, \uparrow\downarrow}(\lambda_{off}, r)$ and

$$G(\lambda_{on}, r) = g_1(\lambda_{on}, r) \frac{d}{dr} Q_{\beta}(\lambda_{on}, r) + g_2(\lambda_{on}, r) Q_{\beta}(\lambda_{on}, r) \quad (6)$$

g_1 and g_2 are sensitivity factors, derived from the integrals over the different line shapes, and Q_{β} is the reciprocal scattering ratio,

$$Q_{\beta} = \frac{\beta_R}{\beta_R + \beta_P}. \quad (7)$$

The main assumptions are [129]:

1. The laser bandwidth is almost negligible.
2. The correction factor G for λ_{off} is negligible due to an appropriate wavelength choice in a range with minimum absorption.

The corrections are important only in the presence of significant aerosol (Sec. 2.4), in particular in the region of pronounced concentration gradients. For a water-vapour DIAL operated in the free troposphere the influence of aerosols is mostly rather small.

The absorption cross sections of water vapour exhibit an altitude-dependent line width due to the spectral broadening as a function of pressure and thermal velocity (Doppler broadening). Two examples of line profiles for lower- and upper-tropospheric conditions are given in Fig. 3. At the same time, the value changes and is significantly higher in the tropopause region than at low altitudes. This results in a growth of the detection sensitivity with altitude, which to some extent counteracts the decreasing humidity. Simulations for a water-vapour DIAL installed at 2765 m a.s.l. showed that the error for upper-tropospheric humidity sounding is reduced by a factor of two in this way [113].

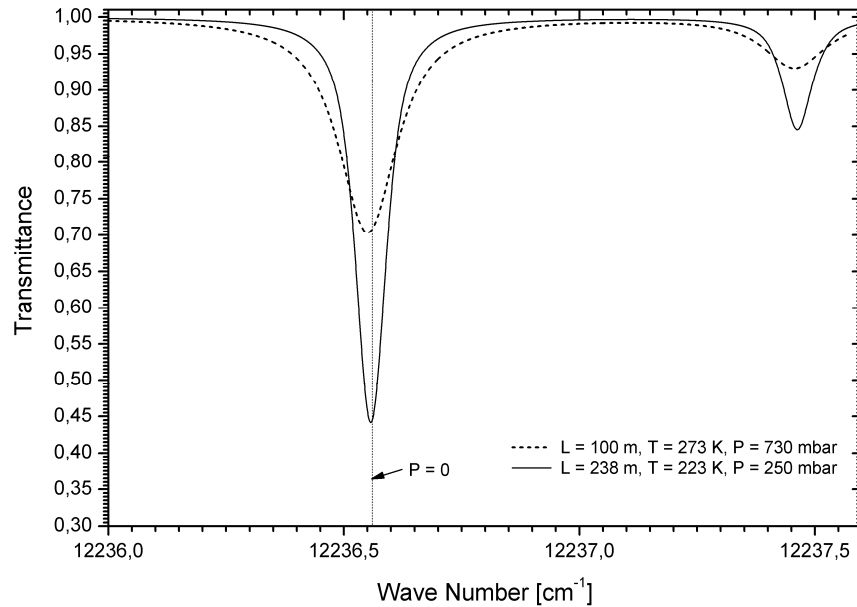


Fig. 3. Transmission spectrum of 1 % water vapour in air at full resolution, calculated with the MOLSPEC 2.2.1 program; the two examples correspond to altitudes of about 2.7 and 10 km. The examples show that the measurement sensitivity grows by at least a factor of two between the lower troposphere and the tropopause region due to the gain in line strength. Just a minor correction of the absorption cross section due to the pressure-induced line shift is required.

Due to the exponential behaviour of the extinction factor in the lidar equation (Eq. 2) an optimum performance of a DIAL can only be achieved within a limited range of distances where the product of the number density of the absorbing species and the absorption cross section is close to optimum. As a consequence, in DIAL systems covering a reasonable range two and more “on” wavelengths are used. In this way a variety of different absorption cross sections can be selected that yield an improved performance at different distances. In the LASE (Lidar Atmospheric Sensing Experiment) water-vapour DIAL system [100] the “on” wavelength of the laser is even tuned into the wing of a line for optimizing the performance for individual humidity conditions [130]. This approach requires a very good knowledge of

the wavelength as well as of the parameters of a spectral line. It is not reasonable in a ground-based system due to the advantage of the sensitivity gain for an operation at the line centre mentioned above.

As already mentioned, a special advantage of air-borne lidar measurements is that the air density grows with distance. Thus, the backscatter signal does not drop as dramatically as in a ground-based lidar. For a water-vapour DIAL this advantage is further enhanced by the strong increase of the humidity with distance.

2.2 Calibration

In the absence of aerosol and quality problems with the backscatter signals, the accuracy of a DIAL system is determined by the accuracy of the absorption cross sections as a function of pressure and temperature. For ozone and water vapour the state of the art for the cross sections has reached a level of about 1 % or better; as could be to some extent also verified by atmospheric intercomparisons. This makes the DIAL method particularly valuable for long-term measurement series in the free troposphere and the stratosphere, where little interference from other trace constituents exists. For a well-aligned DIAL system, both the absolute accuracy and the precision do not change and, as a consequence, no artificial trends are introduced.

Numerous authors have measured the absorption cross sections of ozone in the Hartley-Huggins band system. The differences between the most important listings are small, but not at all negligible. The most accurate measurements were made by Mauersberger et al. [131] and Barnes and Mauersberger [132] at the mercury wavelength 253.7279 nm based on mass-spectrometrically controlling the decomposition of O₃ and the impurities during the measurement. The uncertainty of this value is estimated as ±0.7 %. Daumont et al. [133] and Malicet et al. [134] carefully remeasured the absorption cross section for five different temperatures between 195 and 350 nm (specified errors: 1.1 to 1.5 %) and critically reviewed the deviations from other frequently used data sets. They used pressure and FTIR measurements to control the influence of ozone decomposition on the results and the absence of impurities. The deviations from the 253.7-nm values by Barnes and Mauersberger for the different temperatures are -0.4 % on average. The deviations with respect to the results from the also used data Bass and Paur [135,136] and by L. and M. Molina [137] can be removed by simple rescaling and, in the case of the data by Bass and Paur, also by applying a constant wavelength shift. For the more recent values by Yoshino

et. al. [138] a bias of 1.9 % and a statistical noise of ± 2 % were reported [66].

The ozone DIAL at Garmisch-Partenkirchen (Germany) has been operated with data obtained on request from J. Malicet in 1992 [66]. Routinely, comparisons with the *in-situ* measurements at the nearby Zugspitze summit (2962 m a.s.l.), that are accurate to within less than 1 %, have been made. In the vertical range around this altitude the far-field receiver of the lidar exhibits its best performance. For a selected four-day measurement series with constant westerly advection, ensuring the absence of orographically induced perturbations between the two measurement sites, a standard deviation of 1.6 ppb O₃ (about 2.5 % during that period) was obtained, with an almost not resolvable bias of +0.35 ppb (about 0.6 %).

For H₂O there have been major discrepancies in the near infrared. Older HITRAN versions and the underlying data derived from FTIR measurements [139-142], e.g., exhibit deviations of -10 % from precision measurements with diode-laser spectrometry by Ponsardin and Browell at 817 nm [143]. A much better agreement (+3 % deviation from Ponsardin and Browell's line strengths) is found for the work by Schermaul et al. [144,145]. These data were very recently carefully re-evaluated by Tolchenov and Tennyson [146], including an improved modelling of overlapping lines, and are the basis in the near infrared of the latest HITRAN version (2008) [147]. The bias of 817-nm HITRAN-2008 cross sections with respect to those by Ponsardin and Browell is now just about +1 %, this residual difference, in part, also being caused by the differences in line shapes calculated for the two sets of parameters.

The accuracy of the line parameters in Ref. 143 were verified by the successful validation of LASE [101,148]. An almost perfect agreement, with no resolvable bias, was also established between the ground-based 817-nm DIAL at Garmisch-Partenkirchen [113] and the DLR (Deutsches Zentrum für Luft und Raumfahrt) air-borne 935-nm DIAL [114,115] during the LUAMI (Lindenberg Upper-Air Methods Intercomparisons) campaign in 2008 [149]. This comparison was carried out using both 817 nm line parameters from Ref. 143 and from HITRAN 2008 for the ground-based DIAL, and 935-nm HITRAN 2008 parameters for the DLR system.

2.3 Numerical approaches

General algorithm

There are numerous approaches for computing the trace-gas density from the “on” and “off” backscatter signals. The general algorithm is:

- (1) Subtraction of the background offset from the backscatter profiles
- (2) Numerical smoothing of the noisy backscatter profiles
- (3) Computation of the Rayleigh backscatter coefficients β_R by calculating the air density from radiosonde data or model approximations
- (4) Calculation of the derivative of the DIAL equation and the density of the absorbing species (Eqs. 4 or 5)
- (5) Calculation of the backscatter and extinction coefficients including a molecular-absorption correction based on Step 4
- (6) Calculation of the derivative of the DIAL equation and the density of the absorbing species, including a backscatter and extinction correction; if the new density differ from that in the previous calculation (Step 4) by more than a given tolerance go back to Step 5. Otherwise, go to Step 6.
- (7) Numerical smoothing of the density profile
- (8) Concatenation of density profiles from different data-channels combination
- (9) Minor final smoothing, if necessary

Notes on the algorithm steps:

- (1) This procedure must be made with particular care because of the derivative formation in Eqs. 4 and 5. Minor structures of the background, e.g., due to electromagnetic interference, signal-induced nonlinearities or ringing caused by the detection electronics, result in considerable concentration errors.
- (2) Smoothing can be accomplished in different ways, e.g., by calculating arithmetic mean values of neighboring data bins, by spline or polynomial fits, or by numerical filtering (see following subsection). The raw data should be smoothed only if necessary because a really bad signal-to-noise ratio, taking into account that excessive smoothing can create biases for some of the approaches. In the limit of near-field detection the digital noise dominates and is constant as a function of distance r . A constant smoothing interval should, therefore, be sufficient. In the limit of far-field detection the

- single-photon noise becomes more and more important and dynamically adjusting the smoothing interval can be considered.
- (3) See Chapter 1 “Atmospheric lidar signals and retrieval of aerosol optical characteristics”.
 - (4) There are several ways of computing the derivative in Eqs. 4 and 5. First of all, it is important to note that the logarithm in these expressions leads to a significant bias of the derivative in the presence of noise due to the asymmetry of the noise in logarithmic representation. In the low-signal range, some signals are even negative due to the noise. Instead of reducing the noise in Step 2, it is advisable to modify the computation by

$$\frac{d}{dr} \ln P = \frac{1}{P} \frac{dP}{dr}, \quad \frac{d}{dr} \ln \frac{P_{on}}{P_{off}} = \frac{P_{off}}{P_{on}} \frac{d}{dr} \frac{P_{on}}{P_{off}}. \quad (8)$$

Although the derivative can be calculated from the differences for neighbouring or more distant data points, approaches based on spline or polynomial fits are more elegant. Least-squares fitting of polynomials offer the advantage of a straight-forward determination of the statistical errors by linear operations involving the covariance matrix of the fit [66,150]. Practice has shown that odd-order polynomials are superior. This is explained by symmetry considerations and by the fact that the lowest useful order (straight line) is odd.

For a linear fit and equidistant data points the result of the fits may be expressed in a rather simple formula, resulting in the following solution of the DIAL equation for the i^{th} data point [113]. Selecting a fit interval between data point $i-k$ and $i+k$ one obtains

$$\frac{d}{dr} \ln q_i = \frac{3}{q_i \delta r} \frac{\sum_{j=i-k}^{i+k} (j-i) q_j}{k(k+1)(2k+1)}, \quad (9)$$

$$\text{with } q_i = \frac{P(\lambda_{on}, r_i)}{P(\lambda_{off}, r_i)},$$

δr being the size of the range bin of the transient digitizer or photon-counting system. Application of Eq. 9 allows for a fast computation of the derivative, in particular for constant k , when only the sum in the numerator must be calculated for each step.

- (5) See Sec. 2.4.
- (6) See Step 4.

- (7) Numerical smoothing of the retrieved molecular density is superior to smoothing the raw data (Step 2), because the smoothing requirement can be directly derived from the requirements suggested by the quality of the density profiles. In addition, this approach allows variable adjustment of the smoothing intervals to observed structures in the density profile.
- (8) If several density profiles are calculated from combinations of different data or wavelength channels, the most accurate sections of the individual profiles must be extracted and merged into a single profile representing the respective measurement. This *a-posteriori* concatenation should be preferred to merging the raw data which can produce artifacts. The *a-posteriori* data concatenation includes a quality control.
- (9) Some final smoothing can be applied if small steps remain in the synthesized density profile.

Numerical data smoothing

In this section we briefly present the method applied by Eisele and Trickl [151,152]. Details will soon be published. Numerical low-pass filtering of data points y_i is based on the general equation

$$y'_i = \sum_{j=i-k}^{i+k} a_j y_{i-j} , \quad (10)$$

with the smoothed value y'_i and the coefficients

$$a_j = a_{-j} = N \frac{\sin(2\pi j f_c f_s^{-1})}{j\pi} ,$$

f_c and f_s being the cut-off and sampling frequencies, respectively, and N a normalization factor. The interval width is $L = 2k\delta r$. One general problem with numerical low-pass filtering is the occurrence of ringing. This can be minimized by introducing window functions w_j

$$y'_i = \sum_{j=-k}^k a_j w_j y_{i-j} . \quad (11)$$

After comparing several listed window functions a Blackman-type window [153] was chosen:

$$w_j = 0.42 + 0.50 \cos\left(\pi \frac{j}{k}\right) + 0.08 \cos\left(2\pi \frac{j}{k}\right) . \quad (12)$$

The best performance was achieved by selecting

$$f_c = \frac{f_s}{2k} = \frac{c}{2k\delta r}, \quad (13)$$

c being the speed of light. The response function obtained for applying Eqs. 10 – 13 with $k = 50$ is depicted in Fig. 4 together with that for a sliding arithmetic mean over $2k + 1 = 101$ symmetrically arranged data points. A linear least-squares fit is equivalent to the arithmetic mean, but requires more numerical operations. These linear operations, though suitable for smoothing, are not perfect frequency filters and, therefore, transmit residual high-frequency noise.

If used for evaluating the DIAL equation, a linear fit differs in its step response from that shown in Fig. 4 due to the derivative formation. A nonlinear response with steeper characteristic is obtained.

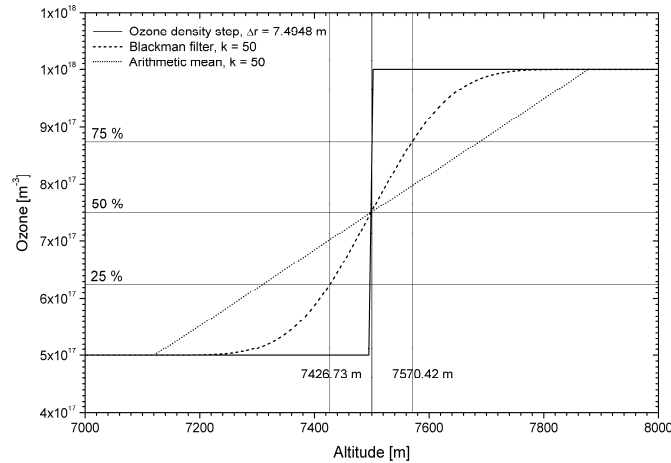


Fig. 4. Response functions for filtering a Heaviside step function with a Blackman-type numerical filter and for a sliding arithmetic mean. The application of a 20-MHz transient digitizer is assumed (i.e., 7.4948-m sampling intervals).

Vertical resolution

There has been substantial incoherence about the definition of the vertical resolution. Most frequently, the length of an averaging or smoothing

interval is taken. This and other kind of approaches can lead to entirely different results, as can be deduced from the response functions in Fig. 4. The German organization Verein Deutscher Ingenieure (VDI), in its DIAL guideline [154], has defined the vertical resolution as the rise of the retrieved density, in response to a Heaviside-type density step, from 25 % to 75 % of the step height. This corresponds to the more conventional full width at half maximum used in the case of isolated features and, therefore, is a reasonable choice. For the examples shown in Fig. 4, one obtains vertical resolutions of 143.69 m (or 19.2 % of the smoothing interval) for the numerical filter and 378.55 m (50.5 %) for the sliding arithmetic mean. For the evaluation of Eq. 9, the range resolution is about 35 % of the full range interval $2k \delta r$ used in a single step of the retrieval.

2.4 Aerosol corrections

Ozone

Aerosol layers and optically thin clouds create pronounced artefacts in DIAL measurements of ozone. The most important interference is caused by the strongly varying particle density, implying in part sharp edges at layer boundaries. In this case, an oscillation of the ozone density is introduced by the derivative in the backscatter term in Eq. 4. The extinction term is less important, but must be considered for visual ranges of roughly less than 30 km. The basic aerosol correction approach for DIAL measurements of ozone was introduced by Browell et al. [155]. The aerosol is derived by an inversion of the backscatter signal for the “off” wavelength, e.g., by the Fernald or Klett methods [156,157]. By using an estimate or a measurement-based approach for the backscatter-to-extinction ratio, B_p , approximate extinction coefficients may be derived from the backscatter coefficient [151]. The corresponding properties for the “on” wavelength are most commonly estimated from those of the “off” wavelength by assuming Ångström laws.

$$\alpha_p(\lambda, r) = \alpha_p(\lambda_0, r) \left(\frac{\lambda}{\lambda_0} \right)^{-\delta}, \quad \beta_p(\lambda, r) = \beta_p(\lambda_0, r) \left(\frac{\lambda}{\lambda_0} \right)^{-\gamma}. \quad (14)$$

These equations may not be exactly fulfilled in certain wavelength ranges, in particular in the UV. However, for backscatter signals of a given wavelength pair, they can always be taken for defining coefficients δ and γ valid for this pair.

The situation is further complicated if the absorption cross section at the “off” wavelength is not negligible. In this case the Klett solution β_K must be modified to

$$\beta_K(\lambda_{\text{off}}, r) = \frac{X(\lambda_{\text{off}}, r) \exp(Y(\lambda_{\text{off}}, r))}{\frac{X(\lambda_{\text{off}}, r_{\text{ref}})}{\beta(\lambda_{\text{off}}, r_{\text{ref}})} + 2 \int_r^{r_{\text{ref}}} \frac{X(\lambda_{\text{off}}, r')}{B_P(\lambda_{\text{off}}, r')} \exp(Y(\lambda_{\text{off}}, r')) dr'}, \quad (15)$$

with

$$X(\lambda, r) = r^2 P(\lambda, r)$$

and

$$Y(\lambda, r) = 2 \int_r^{r_{\text{ref}}} \left(\frac{1}{B_P(\lambda, r')} - \frac{1}{B_R} \right) \beta_R(\lambda, r') dr' - 2 \int_r^{r_{\text{ref}}} \alpha_{O_3}(\lambda, r') dr', \quad (16)$$

where r_{ref} is a reference distance from the system [157]. Initially, this solution is based just on a preliminary (first-order) guess of the ozone distribution, and a second-order ozone distribution must be derived from Eq. 4. The solutions for the backscatter coefficient and the ozone density must be iteratively refined [66]. B_P is mostly assumed to be constant as a function of the wavelength.

From Eq. 4 it is obvious that the aerosol interference becomes low for small wavelength differences. However, this results in a small differential absorption by ozone and, thus, an elevated uncertainty of the retrieved ozone densities. This fact has been frequently ignored in the past and ozone DIAL systems with both too long operating wavelengths and too small wavelength differences have been built. The steepest part of the absorption cross section of ozone is found between roughly 265 nm and 275 nm. Here, simultaneously a high sensitivity for ozone and the smallest interference by the aerosols is obtained. A contour plot visualizing the regions for the best wavelength combinations was published by Völger et al. [158]. Figure 5 shows one example of a measurement at Garmisch-Partenkirchen (Germany, lidar laboratory: 740 m a.s.l.) from Ref. 152, displaying ozone retrievals across the upper edge of the boundary layer together with *in-situ* measurements at the nearby Wank (1780 m a.s.l.) and Zugspitze (2962 m a.s.l.; the two values inserted correspond to times before and after the ozone step had moved across the summit [152]) mountain sites for comparison. Ozone profiles derived from three wavelength combinations are shown: 277 nm and 313 nm, 292 nm and 313 nm, as well as 277 nm and 292 nm. As expected, the combination of the channels with the longest “on” and the longest “off” wavelength yields the highest aerosol-induced error,

and the combination with the smallest “on” wavelength and the smallest “on”-“off” wavelength difference results in an already rather small interference that can be easily corrected. Here, it must be taken into account that the results for 292 nm as the “on” wavelength are smoothed more and, therefore, exhibit a much lower vertical resolution, which even reduces the magnitude of the interference by aerosols. Further details of this figure are explained below.

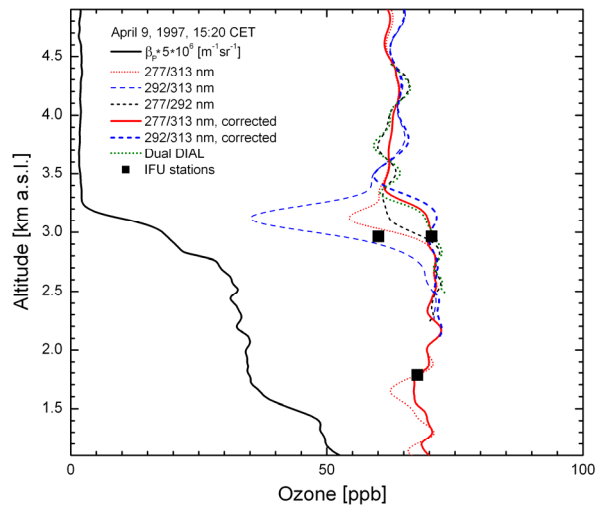


Fig. 5. Influence of aerosol gradients on ozone mixing ratios retrieved from the signals for three different wavelength combinations of the DIAL at Garmisch-Partenkirchen (Germany), in comparison with fully corrected ozone profiles [152]: as expected the largest error is seen for the combination with the longest “on” wavelength. The best performance is obtained for the wavelength pair 277 nm – 313 nm after the correction. This is due to the high sensitivity of the 277-nm measurements to ozone and the better “off” character of the 313-nm data. The results for the DUAL-DIAL method [160] reveal that this method is robust, but slightly suffer above 3.3 km from the lower sensitivity to ozone of the 292-nm data resulting in higher noise. Ozone data for two in-situ stations Zugspitze (2962 m) and Wank (1780) for different times are given for comparison (for details see Ref. 152). Time is given in Central European Time (CET = UTC + 1 h).

A number of approaches for aerosol corrections have been described in the literature. The most attractive schemes are those proposed by Sasano

and Nakane [159], Wang et al. [160] and Trickl and Eisele [152]. Sasano and Nakano take benefit from the use of a three-wavelength DIAL, with two “on” and one “off” wavelength. In this case, three lidar equations are available for determining the wavelength dependences. Wang et al. also assume three-wavelength operation and present a very simple, robust method, named “dual-DIAL technique”, for eliminating the aerosol contribution to the calculated ozone density. After linearizing the wavelength dependences based on Eqs. 14, the ozone density is calculated as the difference of two Eqs. 4, one of them being multiplied with a constant factor C . Selecting this “dual-DIAL” factor as

$$C = \frac{\lambda_{1,on} - \lambda_{1,off}}{\lambda_{2,on} - \lambda_{2,off}} \quad (17)$$

the differences of the correction terms vanish. This approach is applicable as long as there is no additional interference such as absorption of the radiation by other gases. Additional interferences can be removed by applying a different factor C that no longer applies for the aerosols.

Eisele and Trickl [152] give solutions for the correction terms for both two-wavelength and three wavelength DIAL systems. Iterative optimization methods based on evolutionary strategies are introduced. In the three-wavelength method the optical coefficients are optimized by minimizing the difference of the two ozone density profiles retrieved for the two independent wavelength pairs. In the two-wavelength method the correlation of the derivative of the aerosol backscatter coefficient (see the second term of Eq. 4) is minimized. This approach is justified by assuming that such a derivative-type distribution, as observed at the edge of an aerosol layer, is unlikely to occur in the ozone profile. Both methods work very well, but a retrieval of the wavelength dependence of the extinction coefficient is not always possible, since the extinction is frequently low and also a very high quality of the backscatter signals is required.

In Fig. 5 also a comparison of methods of Ref. 150 and the dual-DIAL method is presented. The results of the corrections agree very well, apart from tiny differences in smoothing. The dual-DIAL solution suffers from the fact that the profiles retrieved for 292 nm, due to the lower absorption cross section at this wavelength, are noisier, resulting in “oscillations” that are also seen in the ozone profile for the pair 292 nm – 313 nm.

Water vapour

In the case of water vapour, one of the most surprising facts is that, despite the possibility of narrow spacing of the laser wavelengths, the aerosol contribution re-enters the expression due to the Rayleigh-Brillouin line-broadening effects caused by the backscattering [128,129]. Doppler broadening of the laser light by the aerosols is much smaller than that for Rayleigh backscattering by the atmospheric N₂ and O₂ molecules. To a good approximation, the line shape of the backscattered light is given by:

$$h(\nu, r) = L(\nu) \frac{\beta_P(\nu, r)}{\beta(\nu, r)} + R(\nu, r) \frac{\beta_R(\nu, r)}{\beta(\nu, r)}. \quad (18)$$

L is the frequency distribution of the laser light, R the Rayleigh-Brillouin line shape at distance r, both distributions being normalized to one. The distributions are both centred at the laser frequency, ν . h is part of the extinction term of the lidar equation and, thus, enters the calculation for the downgoing light.

The line shape functions yield the factors g and Q in Eqs. 6 and 7 as described by Bösenberg [129] in a rather complex manner. One example of the correction of a free-tropospheric measurement with slightly elevated aerosol is given by Vogelmann and Trickl [113]. Kiemle et al. found that, even for aerosol-free conditions, the concentration offset caused by the Rayleigh-Brillouin effect at 935 nm varies between 2.9 % at 8 km and 5.2 % at 16 km [114], and, therefore, is not negligible.

2.5 Error considerations and validation

Error estimates have been made by a number of groups (e.g., [58,103,104,114,161-163]). Error sources are a wrong wavelengths or spectroscopic parameters, laser speckle, interference by aerosols or other gases, bad optical alignments, wrong optical design in the presence of an inhomogeneous optical surface (in particular the detectors [164]), detector overload (see Sec. 3.2), fluorescence of optical components (such as interference filters next to a detector [66]), electromagnetic interference and other electronic problems.

In a system free of any of these artefacts detection noise remains the principal source of error. For a receiver optimized for short distances, usually the digitization noise dominates, resulting in a rather constant noise amplitude. In channel optimized for longer distances there is a gradual transition to photon-counting (or shot) noise. Here, a $N^{-1/2}$ dependence of the noise on the number of counts N is a reasonable approximation. The

statistical error can be obtained from an analysis of the data noise. An elegant approach is least-squares fitting of a polynomial to the signal ratio in Eqs. 4 and 5. Here, the statistical error can be directly calculated from the covariance matrix of the fit. If additionally smoothing is applied, the computation of the error propagation becomes more complex.

3. Technical layout

3.1 Laser systems

Powerful laser sources have been used or developed for DIAL applications. The motivation has been achieving an optimum signal-to-noise ratio within a data-acquisition time short enough to account for the atmospheric time scales relevant for the observations. For air-borne applications a reduction of the measurement time is mandatory due to the high speed of the aircraft. High pulse energies are mostly preferred to high repetition rates to reach the same average power in order to reduce the influence of the solar and some of the instrumental background.

Ozone

A variety of laser sources have been used in ozone DIAL systems. Several systems have been based on frequency-doubled dye lasers (e.g., [58,59,75]). This is an important approach for measurements within polluted air masses because the differential absorption of interfering trace gases such as NO₂ and SO₂ can be minimized. UV pulse energies of up to 80 mJ have been demonstrated for such systems [165]. However, the most powerful sources of pulsed UV laser radiation are excimer lasers. Uchino et al. introduced the XeCl excimer laser, emitting at 308 nm, for the measurement of stratospheric ozone [117]. Werner et al. adopted this approach, but added a second (“off”) wavelength, 353 nm, by stimulated Raman shifting in a cell filled with high-pressure hydrogen [55]. In this way the additional costs for a second laser for λ_{off} are avoided.

The absorption cross section of ozone at 308 nm is too low for achieving reasonable detection sensitivity within the troposphere (see Fig. 1), due to the much lower ozone density in this part of the atmosphere. Therefore, KrF lasers have been used as the primary light source by several groups [60,66-70,77,78], in part with a narrow-band oscillator-amplifier design. The pulse energies and repetition rates reach up to 500 mJ and 100 Hz, respectively. Since the emission of KrF laser at 248.5 nm almost

coincides with the absorption maximum of O₃ (Fig. 1) and, thus, implies a significant range reduction, again, stimulated Raman shifting has been used for generating additional wavelengths. High conversion efficiencies of Raman shifting have been reported that reach up to 46 % and 31 %, respectively, for the first- and second-Stokes emission in H₂ at 277.1 nm and 313.2 nm, and 37 % and 15 %, respectively, for the first- and second-Stokes emission in D₂ at 268.4 nm and 291.9 nm [66].

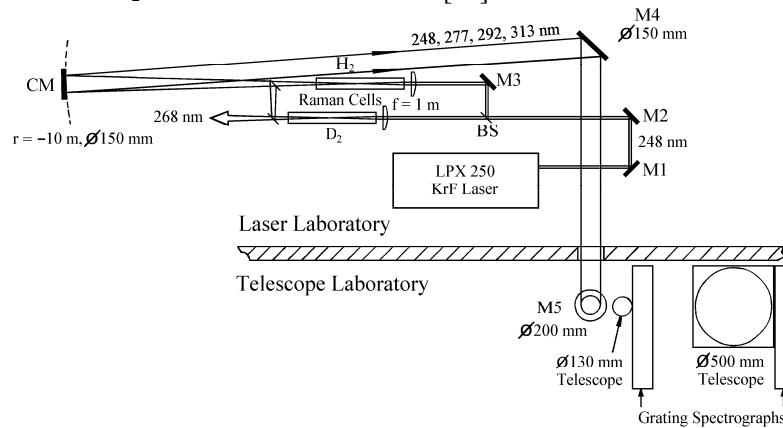


Fig. 6. Stationary ozone DIAL at Garmisch Partenkirchen; a narrow-band KrF laser system with separate oscillator and amplifier is used (linearly polarized, bandwidth 0.2 cm^{-1} , beam divergence 0.2 mrad). Abbreviations: BS: 50 % beam splitter, M1 – M5: mirrors, CM: curved mirror (the diameters of the larger mirrors are specified on the drawing). All transmitted optics are made of CaF₂. 1.1-m grating spectrographs with a spectral resolution of 0.3 nm are used for the wavelength separation and the reduction of the solar background.

An example of a KrF-laser-based ozone lidar system (stationary system in Garmisch-Partenkirchen, Germany [70]) is shown in Fig. 6. 400 mJ from an oscillator-amplifier KrF laser with a bandwidth of 0.2 cm^{-1} , linear polarization and a repetition rate of 99 Hz (Lambda Physik, LPX250) are split into two beams with equal energy. These beams are focussed into H₂ and D₂ Raman cells (pressures: 3 bar and 11 bar, respectively) and recombined, with rather low loss, to transmit radiation at 277.2 nm, 291.9 nm and 313.2 nm, with a custom-made narrow-band pair of beam combiners (Laseroptik GmbH). The linear polarization of the radiation, maintained by using CaF₂ instead of MgF₂ optics, ensures the absence of additional emission lines due to rotational Raman shifting [66]. The beam is subse-

quently expanded to a diameter of more than 0.1 m which limits the beam divergence to angles of 0.5 mrad and less, depending on the Raman gas and Stokes order. Mirrors 1 to 4 are positioned at large distances from the curved output mirror of the laser and the two CaF₂ lenses, in order to avoid damage on optical surfaces by the weak reflections from the output mirror and cell windows.

In addition to the KrF lasers also frequency-quadrupled Nd:YAG lasers have been used (266.1 nm), with UV pulse energies up to 140 mJ. These lasers are more compact and avoid the use of corrosive gases, which is attractive for mobile ozone lidar systems. Raman shifting yields very high first-Stokes conversion efficiencies up to 50 % and 70 % for shifting in D₂ and H₂, in that order, and emission at 289.1 nm and 299.2 nm is generated, respectively, in part using Ar as a buffer gas [65,71]. The wavelength combination 266.1 nm – 299.2 nm is particularly attractive for DIAL measurements in polluted air, with ozone mixing-ratio errors of just 0.01 ppb per ppb of SO₂ and NO₂ [71]. However, the maximum vertical range that can be achieved with 266.1 nm as the “on” wavelength is roughly 3 km (Sec. 4.1), thus requiring a separate detection for short and long distances to improve the detection dynamics.

Also N₂, CO₂ and CH₄ have been used as Raman gases [86,119,120]. The conversion of laser light by stimulated Raman shifting is rather complex and strongly depends on the laser type or model, its beam quality and pulse length. The findings of the different lidar groups have been documented in many publications (e.g., [60-62,65,66,68,73,76,86,119-125]).

Three-wavelength operation has become the state of the art. A computation of ozone from the signal for different wavelength combinations allows for an internal quality control. In addition, interferences may be detected and removed. The lidar operation with a Raman-shifted laser source provides this possibility in an inexpensive way. However, not all wavelength combinations are suitable for ozone measurements in areas with elevated air pollution. As mentioned above here is an important advantage of the frequency-quadrupled Nd:YAG laser.

In addition to the frequency-doubled dye lasers and the Raman shifted fixed frequency lasers, also optical parametric oscillators (OPOs) sum-frequency mixed with 355-nm pump radiation have been used [85]. For idler tuning between 282 nm and 323 nm, pulse energies of 16 to 20 mJ were reported in Ref. 85. More than 30 mJ of tunable UV light (at 30 Hz) between 289 nm and 300 nm for an ozone DIAL were reported by Elsayed et al. [166], who frequency tripled a Ti:sapphire laser outside the wavelength

range of maximum gain. An interesting proposal has been the use of tunable UV sources such as Ce:LiSAF, emitting from 284 to 299 nm [167]. Recently, as much as 98 mJ have been extracted at 290 nm from Ce:LiCaAlF₆ [168].

Water vapour

Due to a particularly wide tuning range in the near IR, covering the three band systems of H₂O mentioned in the preceding subsection, its high output power and its reasonable thermal performance the Ti:sapphire laser has become the preferred laser source for DIAL sounding [100,109,111,113,169] although also alexandrite lasers and OPOs have been used after the end of the dye-laser era [102,103,106,107,110,113-115]. Most systems use laser pumping of Ti:sapphire. As a consequence the output pulse energies are moderate, and only the air-borne LASE system emits more than 100 mJ (up to 150 mJ) per pulse [100]. In contrast to the other systems, the Zugspitze DIAL uses a flashlamp-pumped Ti:sapphire laser currently emitting 250 mJ per pulse, but with potential for much higher pulse energies [113,170].

In order to avoid line shape corrections, the laser bandwidth must be reduced to about one tenth of the absorption line width (≥ 2 GHz) and less. This requires single-longitudinal mode (SLM) operation of the laser. Even more importantly, λ_{on} laser emission outside the absorption line creates a bias. Bösenberg estimates that a spectral purity of the laser system of at least 99.5 % is required for water-vapour measurements with errors less than 3 % [129]. The spectral purity is determined by absorption measurements and was found to exceed this limit significantly for most H₂O DIAL systems.

Different approaches for achieving SLM operation have been reported. The operation of a pulsed SLM Ti:sapphire laser resonator is difficult due to the low gain of the material. Therefore, a reasonable approach is to seed the Ti:sapphire crystals directly with continuous-wave diode lasers [100,169]. This approach, although limiting the wavelength tuning range, is particularly important in mobile or air-borne systems where an efficient active feedback control of the laser frequencies is needed. For the ground-based DIAL system in Hamburg (Germany) [111,169] even unattended long-term operation has been demonstrated [116]. The laser design is shown in Fig. 7. It features a pulse energy of 30 mJ, a frequency bandwidth of 22.5 MHz and a spectral purity (locking efficiency) of 99.95 %. The two DIAL wavelengths are emitted in alternating sequence. A special “ramp-and-fire” technique is used for stabilizing the two laser frequencies: The cavity length is modulated by applying a sine-wave voltage, phase

locked to the pump pulse train, to a piezo transducer attached to one of the mirrors of the ring cavity. In addition, an offset voltage shifts the sine-wave voltage up or down to ensure the correct cavity length at the time of the laser shot.

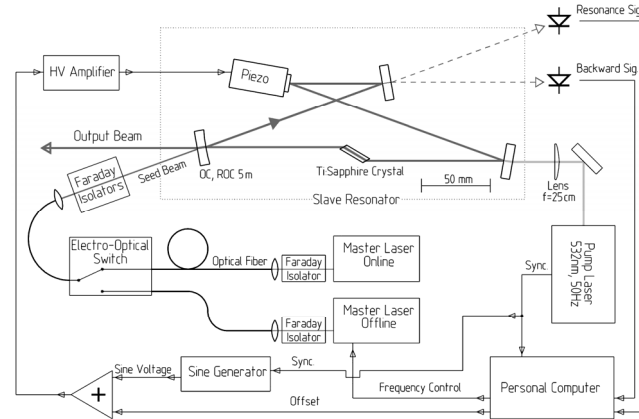


Fig. 7. Laser system of the fully automatic water-vapour lidar system in Hamburg (Max-Planck-Institut für Meteorologie); abbreviations: OC: output coupler, ROC: radius of curvature [169].

In order to overcome the short tuning range of diode lasers, limiting a more general applicability of the lidar, the master oscillators of the Zugspitze DIAL [113] are two pulsed SLM OPOs in Littman cavity configuration (Continuum, Mirage [171]), pumped by a frequency-doubled injection-seeded Nd:YAG laser (Continuum, Powerlite 8020). This approach combines the advantages of a very wide tunability and of a reduction in the number of expensive seed lasers, in particular laser-pumped continuous Ti:sapphire lasers that could also provide a large tuning range. On the other hand, the use of sensitive pulsed oscillators requires higher passive (mechanical and thermal) stability. The OPOs had to be modified for stable single-mode operation and clearly exceeds in performance the commercial version of the OPO [113]. Pulses next to the Fourier-transform limit were obtained: e.g., for near-Gaussian pulses 4.0 ns long, the bandwidth was 130 ± 15 MHz (Fourier limit: 110 MHz). Active frequency locking to a precise interferometer system (Cluster, LM007) is used to keep the laser frequency in the H_2O line centre.

3.2 Receiver design

DIAL is a method limited in quality by background photons, detection noise and nonlinearities in signal processing. Therefore, in practice, the signal-to-noise ratio for the molecules to be detected at long distances does not grow infinitely with the telescope size, and a telescope diameter of the order of 0.5 m is usually sufficient. By contrast, night-time Raman scattering from molecules is background free and, for error-free photon counting, directly yields a signal proportional to the number density of the molecule of interest. Here, a growing telescope size leads to a substantial increase in sensitivity and vertical range. Limitations are given by the costs that explode with size and by the growing difficulty in imaging a large radiation bundle on to a small detector surface.

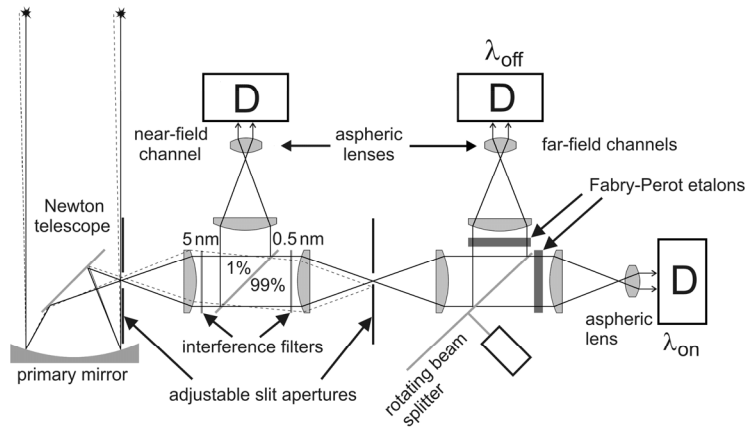


Fig. 8. Example of a receiver design, selected for sequential transmission of “on” and “off” pulses; abbreviation: D means detector; the dashed lines indicate the envelope of a near field return that is blocked at the second aperture. As can be seen from the crossings of the full and the dashed lines the first exit pupil (image plane of the primary mirror) is close to the 99.:1 beam splitter.

The signal drop as a function of distance in a DIAL system with a good near-field coverage (e.g., fully linear return starting at distances near 0.2 km) is extreme for the “on” wavelength. In particular, the dynamic range of the “on” backscatter signal of a ground-based ozone DIAL system covering the boundary layer and altitudes up to about 15 km is eight decades and more. As a consequence, a separation of the large dynamic range into

near-field and far-field detection is important. This can be achieved either by using two separate receivers strongly differing in size, placed at different distances from the outgoing laser beam (e.g., Fig. 6 [66,70]), or by optical beam splitting (e.g., [71,113]). In the second approach, as indicated in Fig. 8 [113], the far-field channel receives at least 99 % of the light, and the near-field return is cut off by an aperture or a blade. Although this method is less complex, it requires an excellent pointing stability of the laser beam in order to avoid a changing position of the blade with respect to the beam and the resulting significant changes in peak signal.

As pointed out in Sec. 3.1 three-wavelength operation with two “on” wavelengths is advisable both for a range extension and for internal quality control. In an ozone DIAL the wavelength separation can conveniently be achieved by using grating spectrographs or interference filters, given the large wavelength spacings (Sec. 3.1). For sequential emission of one or more wavelengths the discrimination of the spectral components is achieved by temporal switching between different data-acquisition channels. This approach is chosen in the example in Fig. 8. Sequential emission is the standard for water-vapour DIAL systems due to the high costs for the SLM lasers, but has also been applied in a mobile ozone DIAL to reduce complexity [71].

The selection of optical and electronic components for a DIAL system must be made with great care in order to avoid any kind of nonlinearity. This is a direct consequence of the density calculation from the derivative of the signal ratio. The results of the retrievals sensitively depends on systematic errors such as electromagnetic interference or ringing on the electronic responses even at a level of less than 50 μV . Optical components should be as far away from focal points as possible as in the example of Fig. 8: for any type of receiving telescope, the imaging of the outgoing laser pulse is accompanied by a spatial scan of the focal points from its near-field to its far-field position. These scans are absent in image planes of the principal mirror. The optical components and, in particular, the detectors [164] should be placed as close as possible to one of these planes. The curved surfaces of lenses must be anti-reflection coated.

As also indicated in Fig. 8, narrow-band interference filters should be mounted in a widened section of the beam in order to minimize changes in transmission angle between the near-field and the far-field light bundle. The equivalent change in wavelength should be smaller than the spectral structures on the filter transmission curve.

An important issue are signal-induced nonlinearities of signals from photomultiplier tubes (PMTs) [172-175]. Two effects are relevant, signal-induced electron emission from a photocathode and overload of the final amplification stages in a PMT, the latter leading to a gain change due to the high-voltage change for the early amplification stages. Signal-induced gain change problems can be reduced by switching the high voltage of one of the dynodes to a lower value during the high-signal phase (“range gating”). Also a variable-gain solution can be found in the literature [176]. However, the cathode-related problems can be only overcome by a careful selection of the PMT. The absence of signal-induced nonlinearities for photon counting and for analogue detection for output signals up to about 40 mV (for 50 Ω termination) has been demonstrated [177] for the Hamamatsu 5600 (new: 7400) PMTs introduced in Refs. 70 and 71.

In the near IR spectral region avalanche photodiodes (APDs) and pin photodiodes are preferred because of the substantial drop in cathode sensitivity of the most convenient PMTs above 800 nm. The selection of the photodiodes must be made with care. Quite frequently, the capacitance is not homogeneous across the entire diode surface which results in slow signal components that are difficult or impossible to compensate. Also, low-noise pre-amplification is rather hard to achieve.

Finally, the digital resolution of the transient digitizers used for recording the analogue signals must be finer than the detection noise. Otherwise, averaged single-bit steps are observed. A solution for minimizing imperfections in digitizers is described in Ref. 178.

4. Some research highlights

DIAL measurements have yielded important contributions to tropospheric research, starting from air-quality studies and extending to the investigation of the impact of long-range transport on the vertical distribution of aerosol, ozone and water vapour above specific regions. This section focusses on a few highlights from ground-based and air-borne measurements.

Two major mechanisms have been discussed to contribute to tropospheric ozone. In recent decades emphasis has been on the growing level of air pollution and its impact on the photo-chemical ozone formation mainly from hydrocarbons and nitric oxides. Many field experiments have been carried out to study the chemical transformation of air masses in and downwind of urban or industrial areas (see Refs. 179-190 for some lidar-related publications and Sec. 4.1). Ozone mixing ratios can rise to more than 80 ppb even at background sites during so-called “ozone episodes” in

summer, with truly hazardous 200 to 300 ppb being reported for some low-latitude megacities, in particular Mexico City [191-193].

The second and most important natural source of ozone is the downward transport from the stratosphere in tropopause folds or cut-off lows [194]. This mechanism has been responsible for the pre-industrial ozone mixing ratios of 10 to 15 ppb [195]. Still, despite strong air pollution due to biomass burning at low latitudes in South America and Africa, the background ozone values in the southern hemisphere are rather low, of about 0 to 25 ppb (e.g., [196-200]). Lidar measurements have greatly contributed to the investigations of stratospheric air intrusions into the troposphere, the significant ozone maxima being an excellent target for vertical sounding. This work has initiated a true renaissance of the investigation of stratosphere-to-troposphere transport (Sec. 4.2) and, in addition, has yielded important contributions to the field of long-range atmospheric transport. Aircraft missions with lidar systems have inferred a lot of information on the distribution and transport of ozone over remote areas (see some of the above citations and Sec. 4.3).

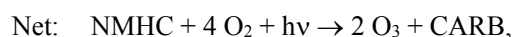
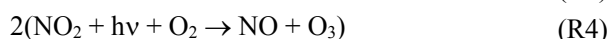
Water vapour is an important complementary tracer, with elevated humidity being characteristic of air from low altitudes and very dry air indicating the presence of upper-tropospheric or stratospheric air. Furthermore, water vapour profiles may yield important information on air-mass mixing in the free troposphere, an issue not yet fully explored. This is highly important since larger-scale models usually overestimate mixing due to their coarse grid size that necessitates averaging of properties.

Vertical profiles of aerosol backscatter coefficients are included in any kind of DIAL system. They may be retrieved from the backscatter signal for the “off” wavelength. In the case of an ozone DIAL, the sensitivity for aerosol is just moderate. This is due to the short wavelengths used, where noise from the strong Rayleigh return masks the aerosol signatures to some extent. This is quite different for the water-vapour DIAL systems that are usually operated at near-IR wavelengths. Aerosol is an excellent indicator of boundary-layer air, though not being fully quantitative due to particle loss by processes such as rainout.

4.1 Examples for air-quality measurements

In areas with elevated pollutant emissions ozone is formed during daytime from precursors, mostly non-methane hydrocarbons (NMHC) and nitric oxides. Solar radiation decomposes ozone yielding electronically

excited (¹D) oxygen atoms that subsequently react with water vapour. This mechanism is the most important source of OH radicals in the troposphere. The formation of ozone is described in the following simplified reaction scheme [201]:



R denoting hydrocarbon radicals and CARB carbonyl compounds. Two ozone molecules are produced for every NMHC oxidized. The cycle of NO and NO₂ (reactions R3 and R4) does not appear in the net equation. The carbonyl compounds may undergo further photochemical reactions that eventually lead to additional ozone formation. The ozone production is highly nonlinear. Liu et al. estimate from model calculations that more than 40 ppb ozone can be generated per ppb NO per day under conditions of low to 1 ppb NO [201]. For high NO this rate gradually diminishes to 10 per day and less. Trainer et al., in an air-quality study for Birmingham (Alabama, U.S.A.), found that approximately seven ozone molecules can be formed per NO_x (= NO + NO₂) molecule added by the urban and power-plant emissions [202].

During the 1995 Southern Oxidants Study in and around Nashville (Tennessee, U.S.A.) an air-borne KrF-laser-based ozone DIAL system, operated by a team from NOAA (National Oceanic and Atmospheric Administration, Boulder, U.S.A.) and NCAR (National Center for Atmospheric Research, Boulder, U.S.A.), helped in localizing and mapping the high-ozone plumes that preferentially form downwind a source area in the presence of wind, but that can also reside over the urban area (with 1.5 million inhabitants) under conditions of full stagnation [183-185]. We pick as an example measurements from July 11, 1995. Before noon the DIAL localized the maximum ozone values (up to about 130 ppb) over Nashville, at altitudes below 1 km. Later on, as shown in Fig. 9, the zone of high O₃ was shifted about 20 to 50 km to the south west in the presence of the north-easterly wind. The peak ozone values between 800 and 1500 m reached at least 150 ppb, which is far above accepted thresholds for health hazards (of the order of 80 ppb).

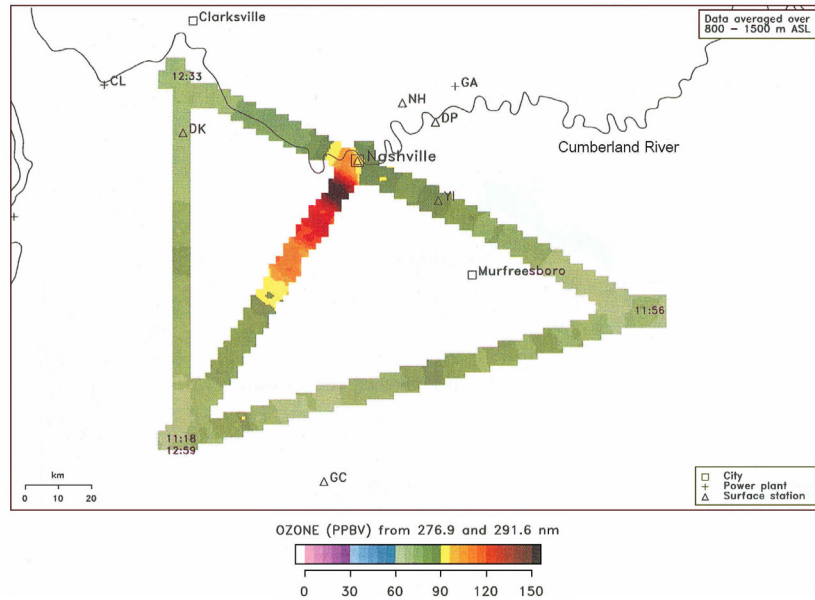


Fig. 9. Ozone mixing ratios averaged from 800 m to 1500 m a.s.l. along a flight track on July 11, 1995, around noon (local summer time); a strong enhancement of boundary-layer ozone downwind of Nashville (Tennessee, U.S.A.) is seen [183]. The times at the turning points of the flights are given in Central Daylight Time (CDT, = UTC - 5 h).

If fresh emissions of NO prevail in the composition of NO_x this can lead to ozone destruction (titration). This could be seen in the plume of the 2.6 GW Cumberland power plant about 100 km west of Nashville (Figs. 10 and 11 [185]). The air-borne ozone DIAL overpassed the plume downwind from the power plant at various distances during the later morning. Over the first 30 km strong ozone depletion to below 10 ppb was registered. At larger distances gradual build-up of O_3 prevailed. On this day (July 7, 1995), the plume stayed within the boundary layer (Fig. 11), which was different during a second flight period (July 19, 1995) with different meteorological conditions.

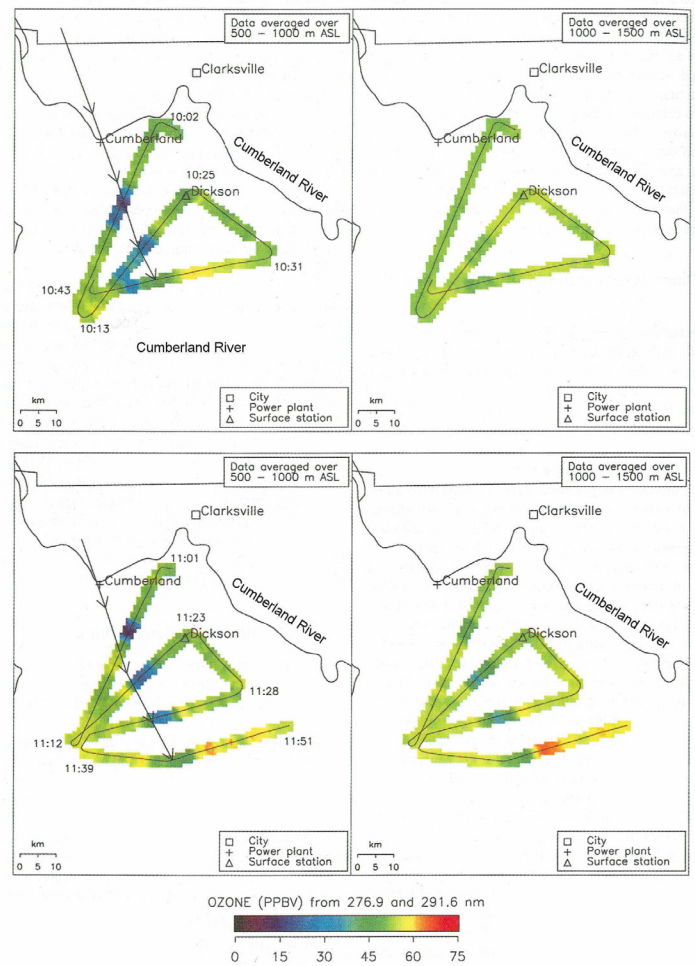


Fig. 10: Ozone mixing ratios averaged from 500 m to 1000 m a.s.l. (left panel) and 1000 m to 1500 m a.s.l. (right panels) along a flight track on July 7, 1995, south of the Cumberland power plant (Tennessee, U.S.A.) for two flight periods in the morning (left and right panels, respectively); along the plume from the power plant a pronounced ozone depletion due to titration was observed, followed by build-up of ozone further downwind [185]. The times at the turning points of the flights are given in Central Daylight

Time (CDT, = UTC - 5 h).

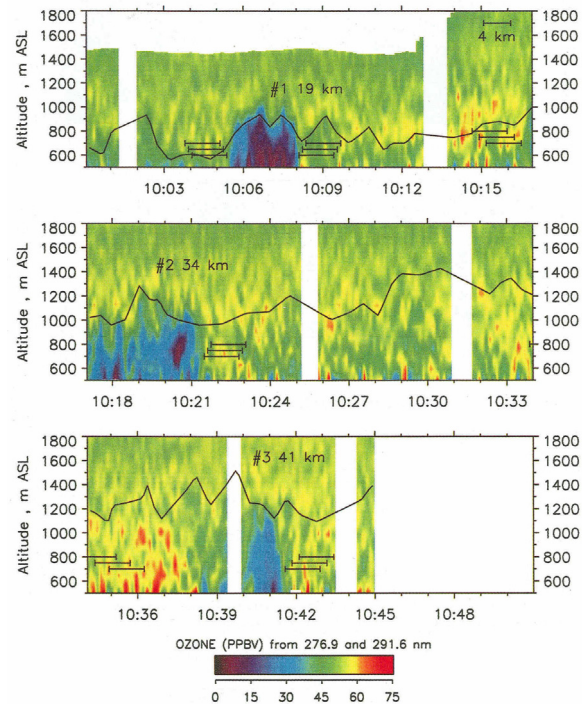


Fig. 11. Ozone mixing ratios from the lidar measurements during the first flight in Fig.10 [185]; in certain parts of the plume complete ozone depletion is seen. The times are given in Central Daylight Time (CDT, = UTC - 5 h).

If mountains are located within 50 to 100 km from an urban area the ozone budget may also be influenced by the orographic wind system streaming towards the mountains during daytime. This flow is mainly generated by up-valley flows inside the mountains (“valley wind”, e.g., [203-205]). This was studied within the VOTALP II (Vertical Ozone Transport in the Alps) “Milano” field campaign in 1998, in a joint effort together with the PIPAPO (Pianura Padana Produzione di Ozono) air-quality campaign around Milano (Italy) [206]. The mobile ozone DIAL from Garmisch-Partenkirchen [71] was operated at Barni (Provincia di Como) within the first mountain range of the Alps about 40 km north of Milano

(Fig. 12) between June 1 and 5, 1998 [207]. On the first four days a day-by-day increase of the afternoon peak ozone advected from the metropolitan area to Barni by the valley wind was observed. During each night the O_3 mixing ratio dropped to roughly 60 ppb due to the reversal of the wind direction.



Fig. 12. Map of the region between Milano (Italy) and the Southern Alps; the Swiss border is marked by the dark-green band (upper left part). The mobile ozone DIAL from Garmisch-Partenkirchen [71] was operated at Barni, between the two "legs" of Lago di Como, next to the upper end of a valley starting at Erba, a town just touching the first upward step of the Alps.

Fig. 13 shows the situation for the day with the highest ozone values, June 4. The behaviour of the ozone rise on the previous days was surprisingly similar, including the bimodal profile at 13:36 CET (Central

European Time = UTC + 1 h). In the late afternoon 120 ppb of ozone were reached, exactly verified by side-by-side measurements with ozone sondes launched by a team from the Swiss Paul-Scherrer Institute. This high mixing ratio turned out to be the limit for retaining an overlap between the near-field and the far-field 266-nm “on” detection channels. No indication of orographic uplifting by the mountain range was observed during most of the day since the lidar was located more on the upwind side of the mountain. However, air-borne trace-gas measurements during the campaign showed some uplifting on the downwind side. The comparison of the DIAL and the sonde measurements also indicates some lifting towards the main part of the lake since the boundary-layer height (defined by elevated ozone) grows as the sonde drifts northward during its ascent. It is interesting to note that the 19:10-CET DIAL profile next to the ground would agree with the sonde profiles for some average position of the two sonde maxima.

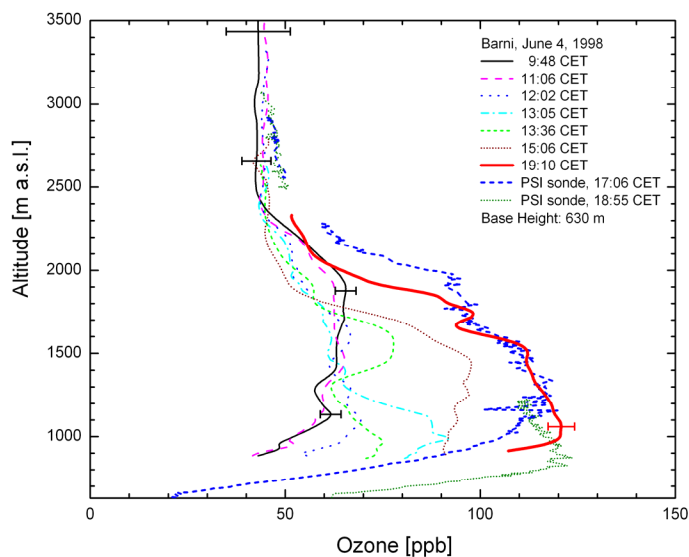


Fig. 13. Vertical profiles of ozone measured at Barni (Como, Italy, see Fig. 12) on June 4, 1998, with the mobile DIAL from IFU (Garmisch-Partenkirchen, [71]) and two ozone sondes launched at the lidar site by a team from the Paul-Scherrer Institute (PSI, Switzerland) at the times specified in the list of curves (sonde data: courtesy of J. Keller, PSI). Only 266 nm was used as the “on” wavelength during that campaign. The times are given in Central European Time (CET, = UTC + 1 h).

4.2 Stratosphere-to-troposphere transport

Lidar measurements (e.g., [149,208-222]) have led to a renaissance in the investigation of stratosphere-to-troposphere transport (STT), the main natural source of tropospheric ozone [194,222]. Full three-dimensional mapping of tropopause folds and the related high-ozone air tongues that may descend even to the lower troposphere, can be achieved by air-borne DIAL measurements of both ozone and water-vapour (e.g., [149,208,215,220]). Ground-based DIAL measurements of the same species yield high-resolution time series of stratospheric intrusion layers transported across the observational area (e.g., [209-214,217-219,221,222]). Due to strongly enhanced ozone concentrations and very low humidity these features are particularly attractive targets for DIAL sounding. Browell et al. even report on lidar observations of aerosols caught in an intrusion layer [208], after the El Chichon volcanic eruption (1982) had loaded the stratosphere with particles that remained there for several years [223,224].

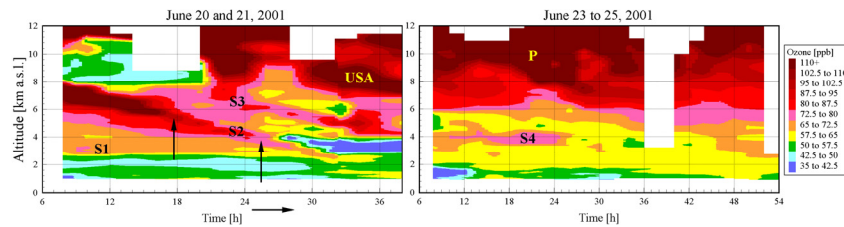


Fig. 14. DIAL measurement series of ozone at Garmisch-Partenkirchen between June 20 and 25, 2001, showing four stratospheric air intrusions (S1-S4) characterized by elevated ozone; the label USA marks air from the boundary layer in the United States, P high-ozone air masses from beyond North America ("Pacific"). The vertical arrows mark the special downward steps in intrusion S2 mentioned in text. The time scale is given in Central European Time (CET = UTC + 1 h).

Tropopause folding mostly occurs in connection with baroclinic waves and upper-level frontogenesis in vicinity of jet streams (e.g., [225]). The horizontal distribution of intrusions is rather inhomogeneous [226]. Deep intrusions in the Northern Hemisphere originate mostly over the north-eastern corner of the large continents. Europe is a major receptor region for intrusions forming over Labrador and Greenland and their neighbourhood. The complexity of intrusion periods can be high, with several stratospheric air tongues co-existing in the troposphere over the North Atlantic and

Europe [222]. This is, e.g., documented in the case of a measurement series with the ozone DIAL at Garmisch-Partenkirchen between June 20 and 25, 2001 [217,222] (Fig. 14) showing as many as four intrusions (labelled as S1 to S4) within just a few days. Two of the intrusions (S2 and S4) are seen in the routine four-day forecast trajectories shown in Fig. 15, S3 is mostly hidden by the trajectories for the other intrusions and S1 is not captured at all since the intrusion occurred far outside the model domain. The series was interrupted on June 22 due to clouds.

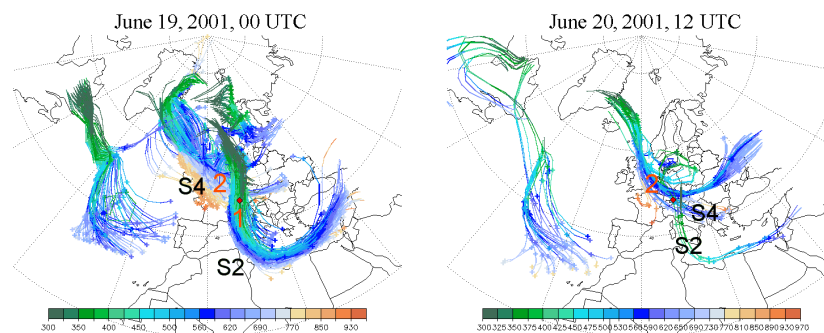


Fig. 15. Selected model forecasts (ETH Zürich [222]) for the period of the measurements shown in Fig. 14, based on four-day forward trajectories released in the stratosphere at the times displayed on the top. The air pressure level, indicating the altitude, is colour coded. Only two of the intrusions (S2 and S3) are seen. The red labels 1 and 2 denote intrusion types introduced in Ref. 220 (anticyclonic and cyclonic arrival, respectively, over Garmisch-Partenkirchen from the area covering Greenland and Iceland).

This lidar measurement series has provided an excellent basis for model validation. Models are used for estimating the vertical exchange budgets between the stratosphere and the troposphere. Still, the estimates of the net annual cross-tropopause ozone flux are rather uncertain since, in principle, a difference of two large numbers must be determined. Also, the stratospheric ozone concentration is introduced from assumptions, such as proportionality to potential vorticity, rather from observational data. However, the meteorological data fields underlying many model simulations have reached a quality allowing the principal features of single intrusions to be calculated. The two most pronounced intrusions in Fig. 14 were well

reproduced with the high-spatial-resolution FLEXPART transport model ([217], Fig. 16). The model was run on meteorological re-analysis data of the European Centre for Medium Range Weather Forecast (ECMWF). The good agreement, in particular in reproducing the two downward steps in intrusion S2 marked by arrows, demonstrates that the meteorological data entering the model are quite adequate for describing the stratospheric air tongue. This version of the figure shows a better agreement in structure with the measurements than that in Ref. 217, which was obtained by averaging over two adjacent grid boxes to adjust the vertical displacement of the modelled structures, caused presumably by a not resolved orography at the northern rim of the Alps.

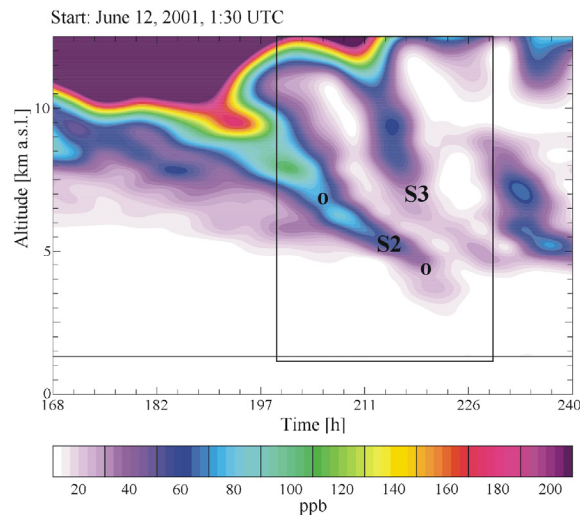


Fig. 16. Simulation with the FLEXPART transport model; the rectangular box corresponds to the left panel in Fig. 15. Only intrusions S2 and S3 are verified, S1 originating outside the model domain [220]. The two downward steps of S2 are nicely reproduced (see circles). The times are given in UTC.

By contrast, a number of Eulerian models tested show lower to really bad agreement [222,227]. The reason is that these models have insufficient spatial resolution, due to covering hemispherical to global scales and including air-chemistry calculations. The best result (from a hemispherical full-year run with the EURAD chemistry-transport model (CTM)) was obtained for the best spatial resolution and shows all four intrusions [222]. Apart from the limitation in spatial resolution, the missing information on

the hemispheric distribution of lower-stratospheric ozone can lead to discrepancies between measured and modelled concentrations.

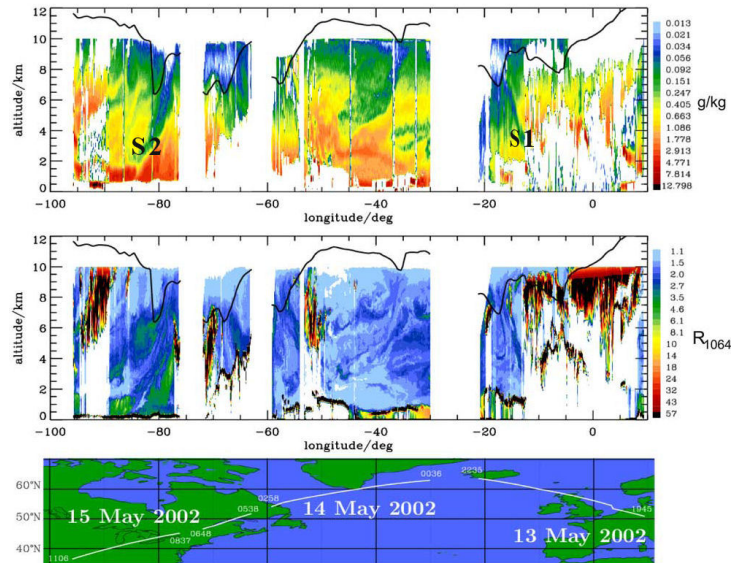


Fig. 17. Water-vapour mass mixing ratios and 1064-nm aerosol scattering ratio R during a flight of the DLR 935-nm DIAL onboard the DLR Falcon aircraft from Germany to the United States [220]; the black lines in the upper two panels represent the dynamical tropopause height (2 pvu contour of the potential vorticity (e.g., [226]); 1 pvu = $10^{-6} \text{ m}^2 \text{ s}^{-1} \text{ K kg}^{-1}$) based on ECMWF analyses. The flight path is shown in the lower panel. S1 and S2 are stratospheric air intrusions.

Flentje et al. report on several stratospheric air intrusions they mapped with their air-borne 935-nm water-vapour DIAL system of DLR during two flights across the Atlantic Ocean [220]. An overview plot from the first flight from Oberpfaffenhofen (Germany) to Oklahoma (U.S.A.) is shown in Fig. 17. The two intrusions (S1 and S2) intersected during that flight can be recognized from the low humidity. A higher-resolution section of S1 is shown in Fig. 18, together with simulations of the curling air tongue in Fig. 19. The mixing ratios inside, deduced from Fig. 18, vary from less than 20 ppm, around 8 km, to about 250 ppm, around 4 km, to compare with fully stratospheric values of roughly 5 ppm reflecting a loss in stratospheric

nature with decreasing altitude. However, the growing mixing ratio cannot be simply explained by mixing of the dry layer with the more humid tropospheric air due to a longer travel in the troposphere. The flight obviously took place transversally to the streamer that exhibits some strong inclination rather than a descent in opposite direction to the flight. As can be seen from Fig. 19 the increase in humidity must be explained by the transverse behaviour of the stratospheric streamer: the influence of mixing with tropospheric air changes across this air tongue.

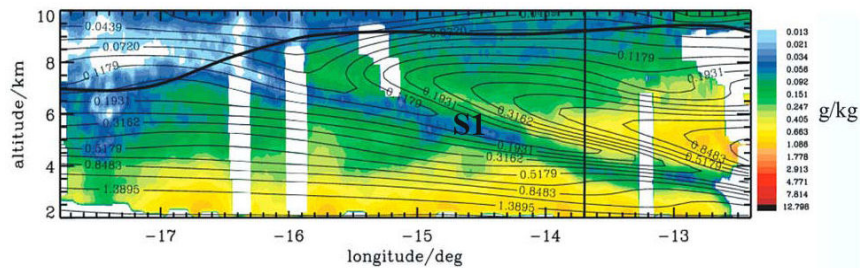


Fig. 18. Water-vapour mass mixing ratios during the approach to Iceland, showing intrusion SI in more detail.

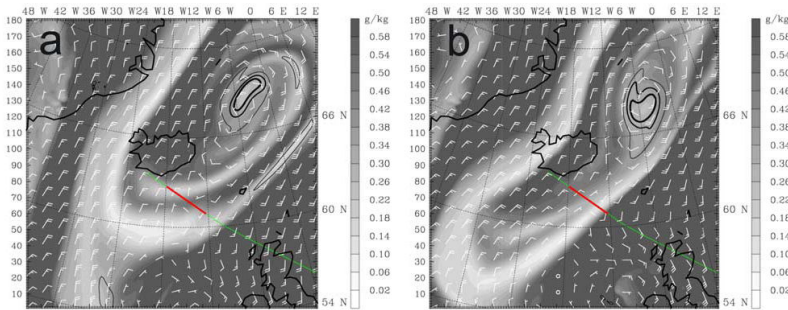


Fig. 19. Model calculation of the water-vapour mass mixing ratio for two times during the flight section shown in Fig. 18, here highlighted in red colour. The intrusion starts in the centre of the top sections of the two figures.

As a matter of fact, the measurements with the free-tropospheric water-vapour DIAL at Garmisch-Partenkirchen have revealed relative humidity (RH) values of typically 2 % and less inside intrusions, after a travel over many thousand kilometres from Greenland to the lidar site. One example of a rather thin stratospheric layer with about 1 % RH, shown with lower vertical resolution in Ref. 113, is depicted in Fig. 20. The corresponding four-day forecast trajectories are displayed in Fig. 21 and

reveal a westward turn prior to the arrival at both Munich and Garmisch-Partenkirchen (roughly 47.5° north). In general the DIAL measurements of ozone and water vapour in the Garmisch-Partenkirchen area, together with the measurements at the in-situ station Zugspitze (2962 m a.s.l.), give evidence that free-tropospheric mixing is very slow. Mixing is clearly overestimated in model calculations due to insufficient spatial resolution.

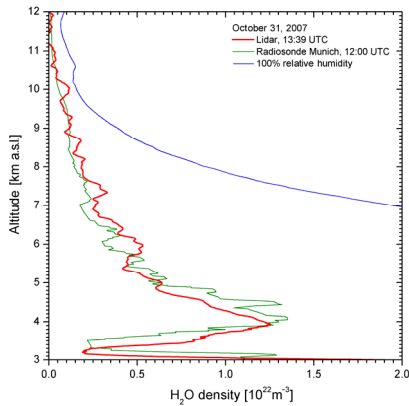


Fig. 20. Water-vapour profiles during a stratospheric intrusion from the DIAL at the Schneefernerhaus research station (2675 m a.s.l., Garmisch-Partenkirchen, 47°N , 11°E) and an RS-92 radiosonde ascent in München-Oberschleißheim ([113]) on October 31, 2007. The radiosonde 100-%-RH profile is given for comparison.

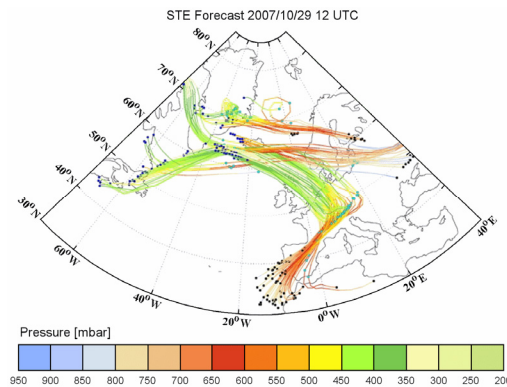


Fig. 21. Four-day forecast trajectories from ETH Zürich for the intrusion shown in Fig. 20; the pressure levels are colour coded. Both stations are inside the same easterly air flow.

4.3 Long-range transport of ozone

The lack of clear evidence of air pollution import from other continents had been a puzzle for long time. The first observation of significant intercontinental transport of ozone, from North America to Europe, was made with a lidar in May 1996 [211,213,219]. The difficulty in surface observations of North-American ozone over Europe is explained by the fact that pronounced layers mostly arrive at altitudes above 3.5 km and, therefore, can rarely be detected even at high-lying atmospheric measurement stations in the Alps. Transport over long distances in the moist marine boundary layer predominantly leads to a loss of ozone. Therefore, observations of ozone from other continents in the lowermost troposphere rarely occur [219].

A case with particularly clear source-receptor relationship from Ref. 211 was analysed by Stohl and Trickl (Figs. 22 and 23) [213]. Here, ozone formed over the eastern United States during a high-pressure period (up to 90 ppb) was exported to the Atlantic by a cold front. The warm conveyor belt of this cold front lifted the polluted air masses to altitudes above 10 km where it was subsequently rapidly transported to Central Europe around a high-pressure zone within the jet stream (see backward trajectories in Fig. 23). At the beginning of the fair-weather period a stratospheric air intrusion descended to the Alpine summit levels, indicated by a band of elevated ozone. This kind of an “inverted atmosphere” with polluted boundary-layer air aloft and stratospheric air near the bottom is characteristic of such an episode and has been found in many lidar time series at Garmisch-Partenkirchen.

The ozone export from North America may be more complex, with contributions from rather different source regions, and the observation of North American ozone layers over Central Europe has, in some cases, continued over several days. The analysis is further complicated by high-ozone plumes (80 to 150 ppb, typically between 5 and 10 km) that arrive with a delay of about two days with respect to the beginning of the fair weather period that were traced back far beyond North America. Recent analyses of these rather reproducible dry air masses have revealed a strong stratospheric component mostly from shallow STT in the vicinity of the subtropical jet stream between North Africa and the Pacific [229]. Some of these plumes contain also Asian and North American air pollution.

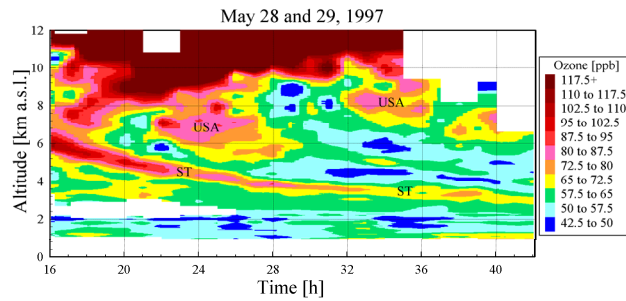


Fig. 22. Time series of tropospheric ozone from lidar measurements at Garmisch-Partenkirchen (Germany) on May 28 and 29, 1997 (revised); simultaneously, ozone import from the stratosphere (ST) and the boundary layer over the eastern United States (USA) is seen [211,213].

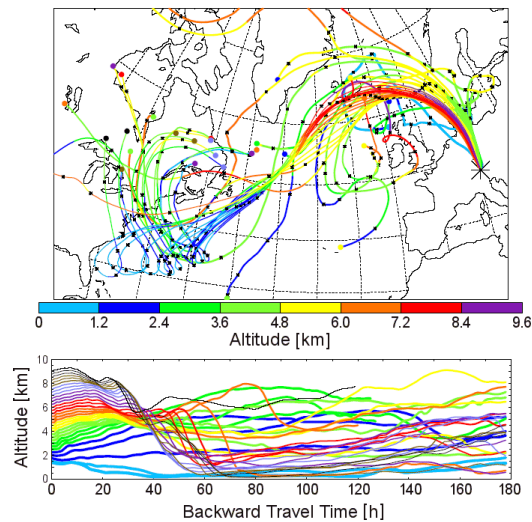


Fig. 23. FLEXTRA backward trajectories started over Garmisch-Partenkirchen (asterisk) on May 29 at 9:00 UTC [213].

The emission of air pollution in East Asia has enormously grown during the recent past. However, the observation of Asian plumes over downwind continents is impeded by the enormous size of the Pacific Ocean. This implies a higher complexity of the transport pathways since more than a single air-mass ascent can take place as that shown for the North Atlantic in

Fig. 23. Alternating cyclonic and anti-cyclonic phases can lead to both ascent and descents, and North America is not necessarily reached. In addition, different air streams merge, such as Asian and stratospheric air (e.g., [230]). However, also rapid trans-Pacific upper-tropospheric transport has been observed [231].

The first observation of Asian air pollution in North America was made at the coastal surface station Cheeka Peak (480 m a.s.l.) in north-western Washington (U.S.A.) in March 1997 [232]. Also trans-Pacific transport of significant amounts of dust from the large Asian deserts have been reported (e.g., [233]).

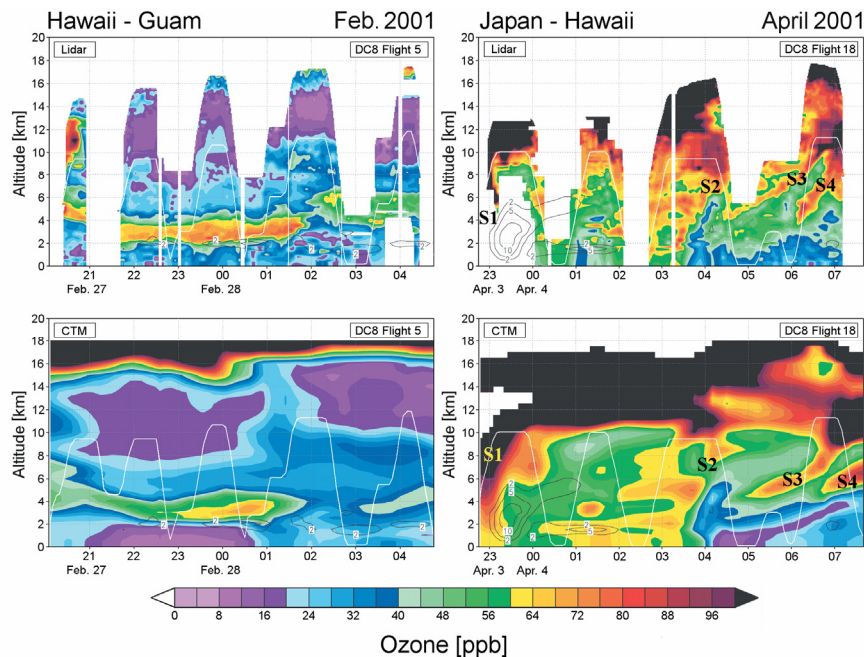


Fig. 24. Lidar and model time-height sections of ozone during two long-distance flights over the Pacific Ocean; the white lines mark the flight tracks [234]. S1 – S4 are stratospheric intrusions. The times are given in UTC.

A great number of large-scale field campaigns have been conducted over the Pacific Ocean. The NASA (National Aeronautics and Space Administration, U.S.A.) air-borne DIAL systems, in numerous flights over different regions of the Pacific, have provided a rich data set on the vertical

distribution of ozone, water vapour and aerosol over these remote areas (e.g., [13,198,199,234-236]). Here, we show in Fig. 24, as examples, results for ozone from two NASA long-distance flights from Hawaii to Guam (flight 5, February 27, 2001) and from Japan to Hawaii (flight 18, April 3-4, 2001), in comparison with results from calculations with a chemistry-transport model (CTM) [234].

During NASA flight 5 from Hawaii to Guam (left panels in Fig. 24) the DIAL detected a thick layer with up to 80 ppb of ozone from Asia that, embedded in low-ozone air, covered a large area over the Pacific between 2 and 4 km. This layer is nicely reproduced by the model calculation, though at lower mixing ratios. The model results are influenced by the emission data available, and, due to the rapidly growing level of air pollution in East Asia, it is reasonable to assume that the concentrations are underestimated as observed. Flight 18 (right panels in Fig. 24) involved two frontal crossings at about 23:30 and 4:00 UTC which result in a pronounced variation of low- and high-ozone regions. More detailed model analyses for different air-mass origins (not shown) reveal continental outflow from Asia of the order of 50 ppb in and ahead (eastward) of the 23:30-UTC front, at altitudes between 2 and 10.5 km. Ahead of the 4:30-UTC front, the model results suggest continental air between 6 and 10 km. Stratospheric air intrusions (S1 – S4) are seen behind the fronts (i.e., on their west side) and towards the end of the flight. This example demonstrates the full complexity of the ozone distribution over these remote oceanic regions.

4.4 Water vapour in the upper troposphere and the lower stratosphere

In spite of the considerable public debate on the climate impact of carbon dioxide, water vapour, due to its atmospheric abundance, is the most important greenhouse gas and contributes two thirds of the greenhouse effect. Any increase in sea-surface temperature results in additional evaporation and potential amplification of the global warming. On the other hand, cloud formation and precipitation could counteract this warming. This complex feedback is far from being quantified.

Lower-tropospheric water vapour prevents radiation in this altitude range from being directly emitted to space. As a consequence, cooling is governed by the humidity above a few kilometres. Thus, accurate sounding of water vapour in the upper troposphere and the lower stratosphere (UTLS) has been called for. This is a demanding task for most techniques used for

routine sounding of water vapour. Balloon-borne radiosondes, although greatly improved in recent years, show limitations at temperatures below 35 °C (e.g., [237]). The data from microwave radiometers cannot be accurately inverted much below 20 km [238]. The same is true also for satellite-borne sensors due to the excessive horizontal averaging.

The DIAL method, in principle, is ideal for reliable long-term water-vapour measurements in the UTLS due to its stable calibration. Also its daytime capability is seen as a plus. However, due to the considerably drop in concentration an observational site at least outside the moist boundary layer is advisable. Such a system is described by Vogelmann and Trickl [113]. By using a 250-mJ/pulse Ti-sapphire laser system and a 0.65-m-diameter receiving telescope, daytime measurements up to 12 km have been demonstrated (e.g., Fig. 20). After improving the laser pulse energy and the detection noise, these authors hope to achieve a UTLS sensitivity limit even below the stratospheric water-vapour volume mixing ratio of 5 ppm.

Routine measurements of stratospheric water vapour with a DIAL are possible by emitting laser radiation in the stronger 935-nm band system of H₂O. However, simulations for average mid-latitude conditions show that such a programme would require a lidar laboratory at about 7.5 km a.s.l. As a consequence, the lidar operation at 935-nm will be restricted to air- [110, 114,115] or space-borne DIAL systems.

References

- [1] M. R. Bowman, A. J. Gibson, M. C. W. Sandford, *Nature* **221**, 456 (1969).
- [2] J. E. Blamont, M. L. Chanin, G. Mégie, *Ann. Geophys.* **26**, 833 (1972).
- [3] C. Granier, J. P. Jegou, G. Mégie, Iron Atoms and Metallic Species in the Earth's upper Atmosphere, *Geophys. Res. Lett.* **16**, 243 (1989).
- [4] E. J. Brinksma, Y. J. Meijer, I. S. McDermid, R. P. Cageao, J. B. Bergwerff, D. P. J. Swart, W. Ubachs, W. A. Matthews, W. Hogervorst, J. W. Hovenier, *Geophys. Res. Lett.* **25**, 51 (1998); Erratum: same issue, p. 521.
- [5] R. M. Schotland, in: Proc. 4th Symposium on Remote Sensing of Environment, University of Michigan, April 12-14; 273, 1966.
- [6] R. M. Schotland, *J. Appl. Meteorol.* **13**, 71 (1974); and references therein.
- [7] R. T. H. Collis, P. B. Russell, in: *Laser Monitoring of the Atmosphere*, E. D. Hinkley, Ed., Springer (Berlin, Heidelberg, New York), 71 (1976).
- [8] R. M. Measures, selected sections in: *Laser Remote Sensing – Fundamentals and Applications*, John Wiley (New York), 510 pp.

- (1984).
- [9] L. Schoulepnikoff, H. van den Bergh, B. Calpini, in: *Encyclopedia of Environmental Analysis and Remediation* **8**, R. A. Meyers, Ed., John Wiley (New York), 4873 (1998).
 - [10] G. G. Gimmestad, in: *Lidar: Range-Resolved Optical Remote Sensing of the Atmosphere*, C. Weitkamp, Ed., Springer (Berlin, Heidelberg, New York), ISBN 0-387-40075-3, 187, 2005.
 - [11] J. Bösenberg, in: *Lidar: Range-Resolved Optical Remote Sensing of the Atmosphere*, C. Weitkamp, Ed., Springer (Berlin, Heidelberg, New York), ISBN 0-387-40075-3, 213, 2005.
 - [12] V. Simeonov, B. Calpini, *Laser Remote Sensing*, T. Fujii and T. Fukuchi, Eds., Taylor & Francis, New York, 123, 2005.
 - [13] E. V. Browell, W. B. Grant, S. Ismail, *Laser Remote Sensing*, T. Fujii and T. Fukuchi, Eds., Taylor & Francis, New York, 723, 2005.
 - [14] Literature on atmospheric measurements with FTIR within the global atmospheric network NDACC (Network for the Detection of Atmospheric Composition Change) may be found at <http://www.ndsc.ncep.noaa.gov/pubs/ftir/>
 - [15] P. F. Ambrico, A. Amodeo, P. Di Girolamo, N. Spinelli, *Appl. Opt.* **39**, 6347 (2000).
 - [16] K. W. Rothe, U. Brinkmann, H. Walther, *Appl. Phys.* **4**, 181 (1974).
 - [17] M. Aldén, H. Edner, S. Svanberg, *Opt. Lett.* **7**, 543 (1982).
 - [18] G. Ancellet, G. Mégie, J. Pelon, R. Capitini, D. Renaut, *Atmos. Environ.* **21**, 2215 (1987).
 - [19] H. Edner, K. Fredriksson, A. Sunesson, S. Svanberg, L. Uneus, W. Wendt, *Appl. Opt.* **26**, 3183 (1987).
 - [20] H. Edner, K. Fredriksson, A. Sunesson, S. Svanberg, L. Uneus, W. Wendt, *Appl. Opt.* **26**, 4330 (1987).
 - [21] H. J. Kölsch, P. Rairoux, J. P. Wolf, L. Wöste, *Appl. Opt.* **28**, 2052 (1989).
 - [22] M. J. Beniston, J. P. Wolf, M. Beniston-Rebetez, H. J. Kölsch, P. Rairoux, L. Wöste, *J. Geophys. Res.* **95**, 9879 (1990).
 - [23] H. Edner, S. Svanberg, *Water, Air, and Soil Pollution* **56**, 131 (1991).
 - [24] C. Weitkamp, P. Bisling, J. Glauer, U.-B. Goers, S. Köhler, W. Lahmann, W. Michaelis, R. Buschner, M. Kolm, W. Birkmayer, Das mobile ortsauflösende Schadgasfernmeßsystem ARGOS, in: Kongreß „LASER91 – Laser in der Umweltmeßtechnik – Laser in Remote Sensing“, available from GKSS-Forschungszentrum Geesthacht G.m.b.H. (Germany) as Report GKSS 91/E/48, 8 pp.

- (1991), in German.
- [25] M. J. J. Milton, P. T. Woods, B. W. Joliffe, N. R. W. Swann, J. T. McIlveen, *Appl. Phys. B* **55**, 41 (1992).
- [26] H. J. Kölsch, P. Rairoux, J. P. Wolf, L. Wöste, *Appl. Phys B* **54**, 89 (1992).
- [27] R. Ferrara, B. E. Maserti, A. De Liso, R. Cioni, B. Raco, G. Taddeucci, H. Edner, P. Ragnarson, S. Svanberg, E. Wallinder, *Chemosphere* **29**, 1421 (1994).
- [28] C. Weitkamp, U.-B. Goers, J. Glauer, S. Köhler, P. Rairoux, F. Immler, L. Wöste, M. Ulbricht, D. Weidauer, *Laser Remote Sensing of Sulfur Dioxide, Nitrogen Dioxide*, in: *Advances in Atmospheric Remote Sensing with Lidar*, A. Ansmann, R. Neuber, and U. Wandinger, Eds., Springer (Berlin, Heidelberg, New York), 411, 1996.
- [29] P. Weibring, H. Edner, S. Svanberg, G. Cecchi, L. Pantani, R. Ferrara, T. Caltabiano, *Appl. Phys. B* **67**, 419 (1998).
- [30] T. Fujii, T. Fukuchi, N. Goto, K. Nemoto, N. Takeuchi, *Appl. Opt.* **40**, 949 (2001).
- [31] M. Dell'Aglio, A. Kholodnykh, R. Lassandro, O. De Pascale, *Opt. Lasers Engin.* **37**, 233 (2002).
- [32] P. Weibring, H. Edner, S. Svanberg, *Appl. Opt.* **42**, 3583 (2003).
- [33] M. Sjöholm, P. Weibring, H. Edner, S. Svanberg, *Opt. Express* **12**, 551 (2004).
- [34] A. C. J. Berkhout, G. R. van der Hoff, J. B. Bergwerff, D. P. J. Swart, A. Hensen, A. Kraai, J. F. M. Huijsmans, J. Mosquera, W. A. J. van Pul, *Measuring Ammonia Emissions from Manured Fields with a Mobile Lidar System*, in: *Reviewed and Revised Papers Presented at the 24th International Laser Radar Conference*, Boulder (Colorado, U.S.A.), June 23-27, 2008, M. Hardesty, S. Mayor, Eds., NOAA and NCAR (2008), ISBN 978-0-615-21489-4, 651 (2008).
- [35] H. Volten, E. J. Brinksma, A. J. C. Berkhout, J. Hains, J. B. Bergwerff, G. R. Van der Hoff, A. Apituley, R. J. Dirksen, S. Calabretta-Jongen, D. P. J. Swart, *J. Geophys. Res.* **114**, D2430, doi: 10.1029/2009JD012441, 18 (2009).
- [36] A. C. J. Berkhout, G. R. van der Hoff, J. B. Bergwerff, D. P. J. Swart, A. Hensen, A. Kraai, J. F. M. Huijsmans, J. Mosquera, W. A. J. van Pul, in: *Reviewed and Revised Papers Presented at the 24th International Laser Radar Conference*, Boulder (Colorado, U.S.A.), June 23-27, 2008, M. Hardesty, S. Mayor, Eds., NOAA and NCAR (2008), ISBN 978-0-615-21489-4, 651 (2008).
- [37] H. Volten, D. P. J. Swart, A. J. C. Berkhout, G. R. Van der Hoff, J. B.

- Bergwerff, Remote Sensing of Nitrogen Dioxide Profiles With the RIVM Mobile Lidar, in: Proceedings of the 8th International Symposium on Tropospheric Profiling, Delft (The Netherlands), October 2009, A. Apituley, H. W. J. Russchenberg, W. A. A. Monna, Eds., RIVM (The Netherlands, <http://cerberus.rivm.nl/ISTP/pages/index.htm>, ISBN 978-90-6960-233-2, Contribution S03-O03, 4 pp. (2009).
- [38] S. Berkhout, R. van der Hoff, D. P. J. Swart, H. Bergwerff, The RIVM Mobile Lidar – Design and Operation of a versatile System for Measuring Atmospheric Trace Gases, <http://www.knmi.nl/omi/research/validation/dandelions/abstractRIVMlidar.pdf> (downloaded 1/2010)
- [39] T. Henningsen, M. Garbuny, R. L. Byer, *Appl. Phys. Lett.* **24**, 242 (1974).
- [40] R. A. Baumgartner, R. L. Byer, *Opt. Lett.* **2**, 163 (1978).
- [41] R. A. Baumgartner, R. L. Byer, *Appl. Opt.* **17**, 3555 (1978).
- [42] N. Menyuk, D. K. Killinger, W. E. DeFeo, *Appl. Opt.* **19**, 3282 (1982).
- [43] E. E. Uthe, *Appl. Opt.* **25**, 2492 (1986).
- [44] R. Barbini, F. Colao, S. Orlando, A. Palucci, S. Ribezzo, in: Proceedings of EUROTRAC Symposium '90, Garmisch-Partenkirchen (Germany), April 2-5, 1990, P. Borrell, B. M. Borrell, W. Seiler, Eds., SPB Academic Publishing (Den Haag), 443 (1991).
- [45] R. Barbini, F. Colao, T. Hermsen, A. Palucci, S. Ribezzo, *Quant. Electron. Plasma Phys.* **20** (1991), 379 (1991).
- [46] N. Menyuk, D. K. Killinger, *Appl. Opt.* **26**, 3062 (1987).
- [47] C. Weitkamp, in: Proceedings of the Fourth International Conference on Infrared Physics, Zürisch (Switzerland), August 22-26, 1988, R. Kesselring, F. K. Kneubühl, Eds., Eidgenössische Technische Hochschule Zürich (Switzerland, 1988); also available from GKSS-Forschungszentrum Geesthacht G.m.b.H. (Germany) as Report GKSS 88/E/45 (1988), ISSN 0344-9626; and references therein, 218 (1988).
- [48] T. D. Gardiner, M. J. T. Milton, F. Molero, P. T. Woods, in: Advances in Atmospheric Remote Sensing with Lidar, A. Ansmann, R. Neuber, P. Rairoux, U. Wandinger, Eds., Springer (Berlin, Heidelberg, New York), ISBN 3-540-61887-2, 451 (1997).
- [49] Y. Zhao, W. A. Brewer, W. L. Eberhard, R. J. Alvarez, *J. Atmos. Ocean. Tech.* **19**, 1928 (2002).
- [50] P. Weibring, H. Edner, S. Svanberg, *Appl. Opt.* **42**, 3583 (2003).
- [51] D. Sakaizawa, C. Nagasawa, T. Nagai, M. Abo, Y. Shibata, M. Nakazato, T. Sakai, *Appl. Opt.* **48**, 748 (2009).

- [52] A. Amediek, A. Fix, G. Ehret, J. Caron, Y. Durand, *Atmos. Meas. Tech.* **2**, 755 (2009).
- [53] K. Ikuta, N. Yoshikane, N. Vasa, Y. Oki, M. Maeda, M. Uchiumi, Y. Tsumura, J. Nakagawa, N. Kawada, *Jpn. J. Appl. Phys.* **38**, 110 (1999).
- [54] J. Pelon, G. Mégie, *Nature* **299**, 137 (1982).
- [55] J. Werner, K. W. Rothe, H. Walther, *Appl. Phys. B* **32**, 113 (1983).
- [56] W. B. Grant, R. D. Hake, *J. Appl. Phys.* **46**, 3019 (1975).
- [57] E. V. Browell, *Opt. Eng.* **21**, 128 (1982).
- [58] J. Pelon, G. Mégie, *J. Geophys. Res.* **87**, 4947 (1982).
- [59] E. V. Browell, A. F. Carter, S. T. Shipley, R. J. Allen, C. F. Butler, M. N. Mayo, J. H. Siviter, W. M. Hall, *Appl. Opt.* **22**, 522 (1983).
- [60] O. Uchino, M. Tokunaga, M. Maeda, Y. Miyazoe, *Opt. Lett.* **8**, 347 (1983).
- [61] G. Ancellet, A. Papayannis, J. Pelon, G. Mégie, *J. Atmos. Oceanic Technol.* **6**, 832 (1989).
- [62] I. S. McDermid, D. A. Haner, M. M. Kleiman, T. D. Walsh, M. L. White, *Opt. Engin.* **30**, 22 (1991).
- [63] Y. Zhao, J. N. Howell, R. M. Hardesty, Transportable Lidar for the Measurement of Ozone Concentration and Flux Profiles in the Lower Troposphere, in: *Proceedings of the 16th International Laser Radar Conference, Cambridge (Massachusetts, U.S.A.), July 20-24, 1992*, 185 (1992)
- [64] E. E. Uthe, J. M. Livingston, *J. Air Waste Manage. Assoc.* **42** (1992), 1313 (1992).
- [65] J. A. Sunesson, A. Apituley, D. P. J. Swart, *Appl. Opt.* **33**, 7045 (1994).
- [66] U. Kempfer, W. Carnuth, R. Lotz, T. Trickl, *Rev. Sci. Instrum.* **65**, 3145 (1994).
- [67] V. S. Buceev, S. K. Vartapetov, I. A. Veselovskii, A. S. Galustov, Y. M. Kovalev, E. S. Svetogorov, S. S. Khmelevtsov, *Appl. Phys. B* **62**, 97 (1996).
- [68] V. S. Buceev, S. K. Vartapetov, I. A. Veselovskii, A. S. Galustov, Y. M. Kovalev, A. Q. M. Prokhorov, E. S. Svetogorov, S. S. Khmelevtsov, C. H. Lee, *Quantum Electronics* **24**, 546 (1994); translated from *Kvantova Electronica* **21**, 591 (1994).
- [69] G. C. Grabbe, J. Bösenberg, H. Dier, U. Görsdorf, V. Matthias, G. Peters, T. Schaberl, C. Senff, *Contr. Atmos. Phys.* **69**, 189 (1996).
- [70] H. Eisele, T. Trickl, in: *Advances in Atmospheric Remote Sensing with Lidar, Selected Papers of the 18th International Laser Radar Conference, Berlin (Germany), July 22 to 26, 1996*, A. Ansmann, R. Neuber, P. Rairoux, U. Wandinger, eds., Springer (Berlin, Heidelberg, New York), 379 (1997).

- [71] P. Brenner, O. Reitebuch, K. Schäfer, T. Trickl, A. Stichternath, in: *Advances in Atmospheric Remote Sensing with Lidar, Selected Papers of the 18th International Laser Radar Conference, Berlin (Germany), July 22 to 26, 1996*, A. Ansmann, R. Neuber, P. Rairoux, U. Wandinger, Eds., Springer (Berlin, Heidelberg, New York), 383 (1997).
- [72] G. Ancellet, F. Ravetta, in: *Advances in Atmospheric Remote Sensing with Lidar, Selected Papers of the 18th International Laser Radar Conference, Berlin (Germany), July 22 to 26, 1996*, A. Ansmann, R. Neuber, P. Rairoux, U. Wandinger, Eds., Springer (Berlin, Heidelberg, New York), 399 (1997).
- [73] E. Wallinder, H. Edner, P. Ragnarson, S. Svanberg, *Physica Scripta* **55**, 714 (1997).
- [74] *Tropospheric Environmental Studies by Laser Sounding (TESLAS)*, in: *Transport and Chemical Transformation of Pollutants in the Troposphere, Vol. 8, Instrument Development for Atmospheric Research and Monitoring*, J. Bösenberg, D. Brassington, and P. C. Simon, Eds., Springer (Berlin, Heidelberg, New York), ISBN 3-540-62516-X, 1 (1997).
- [75] M. H. Proffitt, A. O. Langford, *Appl. Opt.* **36**, 2568 (1997).
- [76] G. Ancellet, F. Ravetta, *Appl. Opt.* **37**, 5509 (1998).
- [77] R. J. Alvarez II, C. J. Senff, R. M. Hardesty, D. D. Parrish, W. T. Like, T. B. Watson, P. H. Daum, N. Gillani, *J. Geophys. Res.* **103**, 31155 (1998).
- [78] I. Veselovskii, B. Barchunov, *Appl. Phys. B* **68**, 1131 (1999).
- [79] J.-L. Baray, J. Leveau, J. Porteneuve, G. Ancellet, P. Keckhut, F. Posny, S. Baldy, *Appl. Opt.* **38**, 6808 (1999).
- [80] V. Matthias, *Vertikalmessungen der Aerosolextinktion und des Ozons mit einem UV-Raman-Lidar*, Dissertation, Universität Hamburg, published as Examensarbeit Nr. 80, Max-Planck-Institut für Meteorologie, Hamburg, Germany, ISSN 0938-5177, 143 pp. (2000), in German.
- [81] G. Vaughan, F. M. O'Connor, D. P. Wareing, *J. Atmos. Chem.* **38**, 295 (2001).
- [82] K. Fritzsche, G. Schubert, *Das Leipziger Festkörper-DAS-LIDAR-System, Gefahrstoffe – Reinhaltung der Luft* **61**, 373 (2001) (in German).
- [83] B. Lazzarotto, M. Frioud, G. Larchevêque, M. Mitev, P. Quaglia, V. Simeonov, A. Thompson, H. van den Bergh, B. Calpini, *Appl. Opt.* **40**, 2985 (2001).

- [84] I. S. McDermid, G. Beyerle, D. A. Haner, T. Leblanc, *Appl. Opt.* **41**, 7550 (2002).
- [85] A. Fix, M. Wirth, A. Meister, G. Ehret, M. Pesch, D. Weidauer, *Appl. Phys. B* **75**, 153 (2002).
- [86] M. Nakazato, T. Nagai, T. Sakai, Y. Hirose, *Appl. Opt.* **46**, 2269 (2007).
- [87] J. L. Machol, R. D. Marchbanks, C. J. Senff, B. J. McCarty, W. L. Eberhard, W. A. Brewer, R. A. Richter, R. J. Alvarez II, D. C. Law, A. M. Weickmann, S. P. Sandberg, *Appl. Opt.* **48**, 512 (2008).
- [88] Tropospheric Environmental Studies by Laser Sounding (TESLAS), in: *Transport and Chemical Transformation of Pollutants in the Troposphere*, Vol. 8, Instrument Development for Atmospheric Research and Monitoring, J. Bösenberg, D. Brassington, and P. C. Simon, Eds., Springer (Berlin, Heidelberg, New York), ISBN 3-540-62516-X, 1 (1997).
- [89] E. R. Murray, R. D. Hake Jr., J. E. van der Laan, J. G. Hawley, *Appl. Phys. Lett.* **28**, 542 (1976).
- [90] E. V. Browell, T. D. Wilkerson, T. J. McIlrath, *Appl. Opt.* **18**, 3474 (1979).
- [91] E. V. Browell, A. F. Carter, T. D. Wilkerson, *Opt. Eng.* **20**, 84 (1981).
- [92] C. Cahen, G. Mégie, P. Flamant, *J. Appl. Meteorol.* **21**, 1506 (1982).
- [93] V. V. Zuev, V. E. Zuev, Y. S. Makushkin, V. N. Marichev, A. A. Mitsel, *Appl. Opt.* **22**, 3742 (1983).
- [94] W. B. Grant, J. S. Margolis, A. M. Brothers, D. M. Tratt, *Appl. Opt.* **26**, 3033 (1987).
- [95] J. Bösenberg, A differential absorption lidar system for high resolution water vapor measurements in the troposphere, Report 71, Max-Planck-Institut für Meteorologie, Hamburg (Germany), 37 pp. (1991).
- [96] G. Ehret, C. Kiemle, W. Renger, G. Simmet, *Appl. Opt.* **32**, 4534 (1993).
- [97] N. S. Higdon, E. V. Browell, P. Ponsardin, B. E. Grossman, C. F. Butler, T. H. Chyba, M. N. Mayo, R. J. Allen, A. W. Heuser, W. B. Grant, S. Ismail, S. D. Mayor, A. F. Carter, *Appl. Opt.* **33**, 6422 (1994).
- [98] C. Senff, J. Bösenberg, G. Peters, *J. Atmos. Ocean. Technol.* **11**, 85 (1994).
- [99] G. Sachse, L. Wang, C. Antill, S. Ismail, E. V. Browell, in: *Optical Remote Sensing of the Atmosphere*, Optical Society of America, 289 (1995).
- [100] A. S. Moore, K. E. Brown, W. M. Hall, J. C. Barnes, W. C. Edwards, L. B. Petway, A. D. Little, W. S. Luck, I. W. Jones, C. W. Antill, E. V. Browell, S. Ismail, in: *Advances in Atmospheric Remote Sensing*

- with Lidar, A. Ansmann, R. Neuber, U. Wandinger, Eds. Springer (Berlin, Heidelberg, New York), 281 (1997).
- [101] E. V. Browell, S. Ismail, W. M. Hall, A. S. Moore, S. A. Kooi, V. G. Brackett, M. B. Clayton, J. D.W. Barrick, F. J. Schmidlin, N. S. Higdon, S. H. Melfi, D. N. Whiteman, in: *Advances in Atmospheric Remote Sensing with Lidar*, A. Ansmann, R. Neuber, U. Wandinger, Eds., Springer (Berlin, Heidelberg, New York), 289 (1997).
- [102] V. Wulfmeyer, *Appl. Opt.* **37**, 3804 (1998).
- [103] V. Wulfmeyer, J. Bösenberg, *Appl. Opt.* **37**, 3825 (1998).
- [104] E. V. Browell, S. Ismail, W. B. Grant, *Appl. Phys. B* **67**, 399 (1998).
- [105] G. Ehret, K. P. Hoinka, J. Stein, A. Fix, C. Kiemle, G. Poberaj, J. *Geophys. Res.* **104**, 31351 (1999).
- [106] D. Bruneau, P. Quaglia, C. Flament, M. Meissonnier, J. Pelon, *Appl. Opt.* **40**, 3450 (2001).
- [107] D. Bruneau, P. Quaglia, C. Flamant, J. Pelon, *Appl. Opt.* **40**, 3462 (2001).
- [108] L. M. Little, G. C. Papen, *Appl. Opt.* **40**, 3417 (2001).
- [109] C. Nagasawa, T. Nagai, M. Abo, Y. Shibata, O. Uchino, in: *Lidar Remote Sensing for Industry and Environment Monitoring*, U. N. Singh, T. Itabe, N. Sugimoto, Eds., *Proc. SPIE* **4153**, 599 (2001).
- [110] G. Poberaj, A. Fix, A. Assion, M. Wirth, C. Kiemle, G. Ehret, *Appl. Phys. B* **75**, 165 (2002).
- [111] K. Ertel, *Application and development of water vapor DIAL systems*, Dissertation (in English), Universität Hamburg, 128 pp. (2004).
- [112] J. L. Machol, T. Ayers, K. T. Schwenz, K. W. Koenig, R. M. Hardesty, C. J. Senff, M. A. Krainak, J. B. Abshire, H. E. Bravo, S. P. Sandberg, *Appl. Opt.* **43**, 3110 (2004).
- [113] H. Vogelmann, T. Trickl, *Appl. Opt.* **47**, 2116 (2008).
- [114] C. Kiemle, M. Wirth, A. Fix, G. Ehret, U. Schumann, T. Gardiner, C. Schiller, N. Sitnikov, G. Stiller, *Atmos. Chem. Phys.* **8**, 5245 (2008).
- [115] M. Wirth, A. Fix, P. Mahnke, H. Schwarzer, F. Schrandt, G. Ehret, *Appl. Phys. B* **96**, 201 (2009).
- [116] H. Linné, Max-Planck-Institut für Meteorologie, Hamburg (Germany), personal communication (2009).
- [117] B. R. Johnson, J. L. Kinsey, *J. Chem. Phys.* **87**, 1525 (1987).
- [118] O. Uchino, M. Maeda, J. Kohno, T. Shibata, C. Nagasawa, M. Hirono, *Appl. Phys. Lett.* **33**, 807 (1978).
- [119] V. Simeonov, V. Mitev, H. Van den Bergh, B. Calpini, *Appl. Opt.* **37**, 7112 (1998).

- [120] D. A. Haner, I. S. McDermid, IEEE J. Quantum Electron. **26**, 1292 (1990).
- [121] V. Simeonov, B. Calpini, H. van den Bergh, in: Lidar Remote Sensing in Atmosphere and Earth Sciences, Reviewed and revised papers presented at the twenty-first International Laser Radar Conference (ILRC21), L. R. Bissonette, G. Roy, and G. Vallée, Eds., Defence R&D Canada – Valcartier, 19 (2002).
- [122] D. Diebel, M. Bristow, R. Zimmermann, Appl. Opt. **30**, 626 (1991).
- [123] M. J. T. Milton, G. Ancellet, A. Apituley, J. Bösenberg, W. Carnuth, F. Castagnoli, T. Trickl, H. Edner, L. Stefanutti, T. Schaberl, A. Sunesson, C. Weitkamp, Appl. Phys. B **66**, 105 (1998).
- [124] L. de Schouepnikoff, V. Mitev, V. Simeonov, B. Calpini, H. Van den Bergh, Appl. Opt. **36**, 5026 (1997).
- [125] A. D. Papayannis, G. N. Tsikrikas, A. A. Serafetinides, Appl. Phys. B **67**, 563 (1998).
- [126] G. Fiocco, J. B. De Wolf, J. Atmos. Sci. **25**, 488 (1968).
- [127] G. Fiocco, G. Benedetti-Michelangeli, K. Maischberger, E. Madonna, Nature **229**, 78 (1971).
- [128] A. Ansmann, J. Bösenberg, Appl. Opt. **26**, 3026 (1987).
- [129] J. Bösenberg, Appl. Opt. **37**, 3845 (1998).
- [130] G. Sachse, L. Wang, C. Antill, S. Ismail, E. V. Browell, in: Optical Remote Sensing of the Atmosphere, Optical Society of America, 289 (1995).
- [131] K. Mauersberger, J. Barnes, D. Hanson, J. Morton, Geophys. Res. Lett. **13**, 671 (1986).
- [132] J. Barnes, K. Mauersberger, J. Geophys. Res. **92**, 14861 (1987).
- [133] D. Daumont, J. Brion, J. Charbonnier, J. Malicet, J. Atmos. Chem. **15**, 145 (1992).
- [134] J. Malicet, D. Daumont, J. Charbonnier, C. Parisse, A. Chakir, J. Brion, J. Atmos. Chem. **21**, 263 (1995).
- [135] A. M. Bass, R. J. Paur, in: Atmospheric Ozone, C. S. Zerefos, A. Ghazi, Eds. D. Reidel (Norwell, Massachusetts, U.S.A.), 606 (1985).
- [136] A. M. Bass, R. J. Paur, in: Atmospheric Ozone, C. S. Zerefos, A. Ghazi, Eds. D. Reidel, (Norwell, Massachusetts, U.S.A.), 1985, 611 (1985).
- [137] L. T. Molina, M. J. Molina, J. Geophys. Res. **91**, 14501 (1986).
- [138] K. Yoshino, J. R. Esmond, D. E. Freeman, W. H. Parkinson, J. Geophys. Res. **98**, 5205 (1993).
- [139] R. A. Toth, J. Mol. Spectrosc. **166**, 176 (1994).
- [140] M-F. Mérienne, A. Jenouvrier, C. Hermans, M. C. A. C. Vandaele, C. Clerbaux, P.-F. Coheur, R. Colin, S. Fally, M. Bach, J. Quant.

- Spectrosc. Radiat. Trans. **82**, 99 (2003).
- [141] L. S. Rothmann, A. Barbe, D. C. Benner, L. R. Brown, C. Camy-Peyret, M. R. Carleer, K. Chance, C. Clerbaux, V. Dana, V. M. Devi, A. Fayt, J.-M. Flaud, R. R. Gamache, A. Goldman, D. Jacquemart, K. W. Jucks, W. J. Lafferty, J.-Y. Mandin, S. T. Massie, V. Nemtchinov, D. A. Newnham, A. Perrin, C. P. Rinsland, J. Schroeder, K. M. Smith, M. A. H. Smith, K. Tang, R. A. Toth, J. Vander Auwera, P. Varanasi, K. Yoshino, *J. Quant. Spectrosc. Radiat. Trans.* **82**, 5 (2003).
- [142] L. S. Rothman, D. Jacquemart, A. Barbe, D. C. Benner, M. Birk, L. R. Brown, M. R. Carleer, C. Chackerian Jr., K. Chance, L. H. Coudert, V. Dana, *J. Quant. Spectrosc. Radiat. Trans.* **96**, 139 (2005).
- [143] P. L. Ponsardin, E. V. Browell, *J. Mol. Spectrosc.* **185**, 58 (1997).
- [144] R. Schermaul, R. C. M. Lerner, D. A. Newnham, R. G. Williams, J. Ballard, N. F. Zobov, D. Belmiloud, J. Tennyson, *J. Mol. Spectrosc.* **208**, 32 (2001).
- [145] R. Schermaul, R. C. M. Lerner, D. A. Newnham, J. Ballard, N. F. Zobov, D. Belmiloud, J. Tennyson, *J. Mol. Spectrosc.* **208**, 43 (2001).
- [146] R. Tolchenov, J. Tennyson, *J. Quant. Spectrosc. Rad. Trans.* **109**, 559 (2008).
- [147] L. S. Rothmann, I. E. Gordon, A. Barbe, D. C. Benner, P. F. Bernath, M. Birk, V. Boudon, L. R. Brown, A. Campargue, C.-P. Champion, K. Chance, L. H. Coudert, V. Dana, V. M. Devi, S. Fally, J.-M. Flaud, R. R. Gamache, A. Goldman, D. Jacquemart, I. Kleiner, N. Lacome, W. J. Lafferty, J.-Y. Mandin, S. T. Massie, S. N. Mikhailenko, C. E. Miller, N. Moazzen-Ahmadi, O. V. Naumenko, A. V. Nikitin, J. Orphal, V. I. Perevalov, A. Perrin, A. Predoi-Cross, C. P. Rinsland, M. Rotger, M. Simečková, M. A. H. Smith, K. Sung, S. A. Tashkun, J. Tennyson, R. A. Toth, A. C. Vandaele, J. Vander Auwera, *J. Quant. Spectrosc. Radiat. Trans.* **110**, 533 (2009).
- [148] R. A. Ferrare, E. V. Browell, S. Ismail, S. A. Kooi, L. H. Brasseur, V. G. Brackett, M. B. Clayton, J. D. W. Barrick, D. S. Diskin, J. E. M. Goldsmith, B. M. Lesht, J. R. Podolske, G. W. Sachse, F. J. Schmidlin, D. D. Turner, D. N. Whiteman, D. Tobin, L. M. Miloshevich, H. E. Revercomb, B. B. Demoz, P. Di Girolamo, *J. Atmos. Oceanic Technol.* **21**, 1790 (2004).
- [149] M. Wirth, A. Fix, G. Ehret, J. Reichardt, R. Begie, D. Engelbart, H. Vömel, B. Calpini, G. Romanens, A. Apituley, K. M. Wilson, H. Vogelmann, T. Trickl, in: *Proceedings of the 8th International*

- Symposium on Tropospheric Profiling (ISTP2009), A. Apituley, H. W. J. Russchenberg, W. A. A. Monna, Eds., RIVM (The Netherlands), <http://cerberus.rivm.nl/ISTP/pages/index.htm>, ISBN 978-90-6960-233-2, 3 pp. (2009).
- [150] U. Kempfer, Entwicklung und Anwendung eines differentiellen Absorptions-LIDAR-Systems zur Messung der troposphärischen Ozonkonzentration, Dissertation, Universität München, 151 pp. (1992), in German.
- [151] H. Eisele, Aufbau und Betrieb eines Dreiwellenlängen-Lidars für Ozonmessungen in der gesamten Troposphäre und Entwicklung eines neuen Auswerteverfahrens zur Aerosolkorrektur, Dissertation, Universität Tübingen (1997), published as Schriftenreihe des Fraunhofer-Instituts für Atmosphärische Umweltforschung **55** (Verlag Dr. W. Maraun, Frankfurt/Main, Germany), ISBN 3-932666-08-9, 107 pp. (1998), in German.
- [152] H. Eisele, T. Trickl, *Appl. Opt.* **44**, 2638 (2005).
- [153] R. B. Blackman, J. W. Tukey, in: *The Measurement of Power Spectra, From the Point of View of Communications Engineering*, Dover Publications, New York, U.S.A., 95 (1959).
- [154] VDI guide line 4210, Measuring gaseous air pollution with the DAS LIDAR, Verein Deutscher Ingenieure, Düsseldorf, Germany, 47 (1999).
- [155] E. V. Browell, S. Ismail, S. T. Shipley, *Appl. Opt.* **24**, 2827 (1985).
- [156] F. G. Fernald, *Appl. Opt.* **23**, 652 (1984).
- [157] J. D. Klett, *Appl. Opt.* **24**, 1638 (1985).
- [158] P. Völger, J. Bösenberg, I. Schult, *Beitr. Phys. Atmosph.* **69**, 177 (1996).
- [159] Y. Sasano, H. Nakane, S. Hayashida-Amano, N. Sugimoto, I. Matsui, in *Ozone in the Atmosphere*, R. D. Bojkov, P. Fabian, Eds., A. Deepak Publishing, Hampton (Virginia, U.S.A.), 746 (1989).
- [160] Z. Wang, H. Nakane, H. Hu, J. Zhou, *Appl. Opt.* **36**, 1245 (1997)
- [161] A. Papayannis, G. Ancellet, J. Pelon, G. Mégie, *Appl. Opt.* **29**, 467 (1990).
- [162] V. Wulfmeyer, C. Walther, *Appl. Opt.* **40**, 5304 (2001).
- [163] V. Wulfmeyer, C. Walther, *Appl. Opt.* **40**, 5321 (2001).
- [164] V. Simeonov, G. Larcheveque, P. Quaglia, H. Van den Bergh, B. *Appl. Opt.* **28**, 5186 (1999).
- [165] K. S. E. Eikema, W. Ubachs, W. Vassen, W. Hogervorst, *Phys. Rev A* **55**, 1866 (1997).
- [166] K. A. Elsayed, S. Chen, L. B. Petway, B. L. Meadows, W. D. Marsh, W. C. Edwards, J. C. Barnes, R. J. DeYoung, *Appl. Opt.* **41**, 2734 (2002).

- [167] R. Rambaldi, M. Douard, J.-P. Wolf, *Appl. Phys. B* **61**, 117 (1995).
- [168] S. Ono, Y. Suzuki, T. Kozeki, H. Murakami, H. Ohtake, N. Sarukura, H. Sato, S. Machida, K. Shimamura, T. Fukuda, *Appl. Opt.* **41**, 7556 (2002).
- [169] K. Ertel, H. Linné, J. Bösenberg, *Appl. Opt.* **44**, 5120 (2005).
- [170] A. Hoffstädt, I.E.E.E. *J. Quantum Electron.* **33**, 1850 (1997).
- [171] W. R. Bosenberg, D. R. Guyer, *J. Opt. Soc. Am. B* **10**, 1716 (1993).
- [172] Y. Iikura, N. Sugimoto, Y. Sasano, H. Shimzu, *Appl. Opt.* **26**, 5299 (1987).
- [173] M. P. Bristow, D. H. Bundy, A. G. Wright, *Appl. Opt.* **34**, 4437 (1995).
- [174] C. K. Williamson, R. J. De Young, *Appl. Opt.* **39**, 1973 (2000).
- [175] M. Bristow, *Appl. Opt.* **41**, 4975 (2002).
- [176] S. Lehmann, V. Wulfmeyer, J. Bösenberg, *Appl. Opt.* **36**, 3469 (1997).
- [177] S. Kreipl, Messung des Aerosoltransports am Alpennordrand mittels Laserradar (Lidar), Dissertation, University of Erlangen (Germany), 195 pp. (2006), in German.
- [178] A. O. Langford, *Appl. Opt.* **34**, 8330 (1995).
- [179] E. Durieux, L. Fiorani, B. Calpini, M. Flamm, L. Jaquet, H. van den Bergh, *Atmos. Environ.* **32**, 2141 (1998).
- [180] L. Fiorani, B. Calpini, L. Jaquet, H. van den Bergh, E. Durieux, *Atmos. Environ.* **32**, 2151 (1998).
- [181] Y. Zhao, R. D. Marchbanks, C. J. Senff, H. D. Johnson, in: Ninetenth International Laser Radar Conference, Annapolis (Maryland, U.S.A.), July 6-10, 1998, U. N. Singh, S. Ismail, and G. K. Schwemmer, Eds., NASA Langley Research Center (1998), NASA/CP-1998-207671/PT1, 375 (1998).
- [182] R. M. Banta, C. J. Senff, A. B. White, M. Trainer, R. T. McNider, R. J. Valente, S. D. Mayor, R. J. Alvarez, R. M. Hardesty, D. Parrish, F. C. Fehsenfeld, *J. Geophys. Res.* **103**, 22519 (1998).
- [183] R. J. Valente, R. E. Imhoff, R. L. Tanner, J. F. Meagher, P. H. Daum, R. M. Hardesty, R. M. Banta, R. J. Alvarez, R. T. McNider, N. V. Gillani, *J. Geophys. Res.* **103**, 22555 (1998).
- [184] C. J. Senff, R. M. Hardesty, R. J. Alvarez II, S. D. Mayor, *J. Geophys. Res.* **103**, 31173 (1998).
- [185] A. Thomasson, S. Geffroy, E. Frejafon, D. Weidauer, R. Fabian, Y. Godet, M. Nominé, T. Ménard, P. Rairoux, D. Moeller, J. P. Wolf, *Appl. Phys. B* **74**, 453 (2002).
- [186] K. Kourtidis, C. Zerefos, S. Rapsomanikis, V. Simeonov, B. Balis, P. E. Perros, A. M. Thompson, J. Witte, B. Calpini, W. M. Sharobiem,

- A. Papayannis, N. Mihalopoulos, R. Drakou, J. Geophys. Res. **107**, 8140, doi: 10.1029/2000JD000140, PAU 7, 13 pp. (2002).
- [187] O. Duclaux, E. Fejafon, H. Schmidt, A. Thomasson, D. Mondelain, J. Yu, C. Guillaumont, C. Puel, F. Savoie, P. Ritter, J. P. Boch, J. P. Wolf, Atmos. Environ. **35**, 5081 (2002).
- [188] O. Couach, I. Balin, R. Jiménez, P. Ristori, S. Perego, F. Kirchner, V. Simeonov, B. Calpini, H. van den Berg, Atmos. Chem. Phys. **3**, 549 (2003).
- [189] A. Dufour, M. Amodei, G. Ancellet, V.-H. Peuch, Atmos. Res. **74**, 161 (2005).
- [190] V. Simeonov, P. Ristori, M. Taslakov, T. Dineev, L. T. Molina, M. J. Molina, H. van den Bergh, Proc. SPIE **5984**, 59840O-1, 6 pp. (2005).
- [191] Data from the air-quality monitoring network of Mexico City can be accessed at http://www.sma.df.gob.mx/simat/home_base.php
- [192] X. Tie, S. Madronich, G.-H. Li, Z. Ying, R. Zhang, A. R. Garcia, J. Lee-Taylor, Y. Liu, Atmos. Environ. **41**, 1989 (2007).
- [193] A. Minga, V. Thouret, M. Saunois, C. Delon, D. Serça, C. Mari, B. Sauvage, A. Mariscal, M. Leriche, B. Cros, Atmos. Chem. Phys. **10**, 895 (2010); and references therein.
- [194] G.-J. Roelofs, J. Lelieveld, Tellus B **49**, 38 (1997).
- [195] A. Volz, D. Kley, Nature **332**, 240 (1988).
- [196] H. B. Singh, G. L. Gregory, B. Anderson, E. Browell, G. W. Sachse, D. D. Davis, J. Crawford, J. D. Bradshaw, R. Talbot, D. R. Blake, D. Thornton, R. Newell, J. Merrill, J. Geophys. Res. **101**, 1907 (1996).
- [197] D. Kley, P. J. Crutzen, H. G. J. Smit, H. Vömel, S. Oltmans, H. Grassl, V. Ramanathan, Science **274**, 230 (1996).
- [198] E. V. Browell, M. A. Fenn, C. F. Butler, W. B. Grant, J. T. Merrill, R. E. Newell, J. D. Bradshaw, S. T. Sandholm, B. E. Anderson, A. R. Bandy, A. S. Bachmeier, D. R. Blake, D. D. Davis, G. L. Gregory, B. G. Heikes, Y. Kondo, S. C. Liu, F. S. Rowland, G. W. Sachse, H. B. Singh, R. W. Talbot, D. C. Thornton, J. Geophys. Res. **111**, 1691 (1996).
- [199] E. V. Browell, M. A. Fenn, C. F. Butler, W. B. Grant, S. Ismail, R. A. Ferrare, S. A. Kooi, V. G. Brackett, M. B. Clayton, M. A. Avery, J. D. W. Barrick, H. E. Fuelberg, J. C. Maloney, R. E. Newell, Y. Zhu, M. J. Mahoney, B. E. Anderson, D. R. Blake, W. H. Brune, B. G. Heikes, G. W. Sachse, H. B. Singh, R. W. Talbot, J. Geophys. Res. **106**, 32481 (2001).
- [200] S. J. Oltmans, A. S. Lefohn, J. M. Harris, I. Galbally, H. E. Scheel, G. Bodeker, E. Brunke, H. Claude, D. Tarasick, B. J. Johnson, P. Simmonds, D. Shadwick, K. Anlauf, K. Hayden, F. Schmidlin, F.

- Fujimoto, K. Akagi, C. Meyer, S. Nichol, J. Davies, A. Redondas, E. Cuevas, Long-term changes in tropospheric ozone, *Atmos. Environ.* **40**, 3156 (2006).
- [201] S. C. Liu, M. Trainer, F. C. Fehsenfeld, D. D. Parrish, E. J. Williams, D. W. Fahey, G. Hübler, P. C. Murphy, *J. Geophys. Res.* **92**, 4191 (1987).
- [202] M. Trainer, B. A. Ridley, M. P. Buhr, G. Kok, J. Walega, G. Hübler, D. D. Parrish, F. C. Fehsenfeld, *J. Geophys. Res.* **100**, 18823 (1995).
- [203] I. Vergeiner, E. Dreiseitl, *Atmos. Phys.* **36**, 264 (1987).
- [204] M. Furger, J. Dommen, W. K. Graber, L. Pioggio, A. Prévôt, S. Emeis, G. Grell, T. Trickl, B. Gomiscek, B. Neininger, G. Wotawa, *Atmos. Environ.* **34**, 1395 (2000).
- [205] W. Carnuth, T. Trickl, *Atmos. Environ.* **34**, 1425 (2000).
- [206] A. Neftel, C. Spirig, A. S. H. Prévôt, M. Furger, J. Stutz, B. Vogel, J. Hjorth, *J. Geophys. Res.* **107**, 8188, doi:10.1029/2001JD001263, LOP 1, 10 pp. (2002).
- [207] T. Trickl, in: TOR-2, Tropospheric Ozone Research, EUROTRAC-2 Subproject Final Report, A. Lindskog, Subproject Co-ordinator, EUROTRAC-2 International Scientific Secretariat, GSF – Forschungszentrum für Umwelt und Gesundheit (München, Germany), 146 (2003).
- [208] E. V. Browell, E. F. Danielsen, S. Ismail, G. L. Gregory, S. M. Beck, *J. Geophys. Res.* **92**, 2112 (1987).
- [209] G. Ancellet, J. Pelon, M. Beekmann, A. Papayannis, G. Mégie, *J. Geophys. Res.* **96**, 22401 (1991).
- [210] A. O. Langford, C. D. Masters, M. H. Proffitt, E. Y. Hsie, A. F. Tuck, *Geophys. Res. Lett.* **23**, 2501 (1996).
- [211] H. Eisele, H. E. Scheel, R. Sladkovic, T. Trickl, *J. Atmos. Sci.* **56**, 319 (1999).
- [212] F. Ravetta, G. Ancellet, J. Kowol-Santen, R. Wilson, D. Nedeljkovic, Ozone, *Monthly Weather Review* **127**, 2641 (1999).
- [213] A. Stohl, Trickl, *J. Geophys. Res.* **104**, 30445 (1999).
- [214] J.-L. Baray, V. Daniel, G. Ancellet, B. Legras, *Geophys. Res. Lett.* **27**, 353 (2000).
- [215] W. B. Grant, E. V. Browell, C. F. Butler, M. A. Fenn, M. B. Clayton, J. R. Hannan, H. E. Fuelberg, D. R. Blake, N. J. Blake, G. L. Gregory, B. G. Heikes, G. W. Sachse, H. B. Singh, J. Snow, R. W. Talbot, *J. Geophys. Res.* **105**, 3757 (2000).
- [216] J. Y. N. Cho, R. E. Newell, E. V. Browell, W. B. Grant, C. F. Butler,

- M. A. Fenn, *Geophys. Res. Lett.* **28**, 3243 (2001).
- [217] P. Zanis, T. Trickl, A. Stohl, H. Wernli, O. Cooper, C. Zerefos, H. Gaeggeler, A. Priller, C. Schnabel, H. E. Scheel, H.-J. Kanter, L. Tobler, P. W. Kubik, P. Cristofanelli, C. Forster, P. James, E. Gerasopoulos, A. Delcloo, A. Papayannis, H. Claude, *Atmos. Chem. Phys.* **3**, 763 (2003).
- [218] E. Galani, D. Balis, P. Zanis, C. Zerefos, A. Papayannis, H. Wernli, E. Gerasopoulos, *J. Geophys. Res.* **108**, 8527, doi: 10.1029/2002JD002596, STA 12, 10 pp. (2003).
- [219] T. Trickl, O. C. Cooper, H. Eisele, P. James, R. Mücke, A. Stohl, *J. Geophys. Res.* **108**, 8530, doi:10.1029/2002JD002735, STA 15, 23 pp. (2003).
- [220] H. Flentje, A. Dörnbrack, G. Ehret, A. Fix, C. Kiemle, G. Poberaj, M. Wirth, *J. Geophys. Res.* **110**, D03115, doi: 10.1029/2004JD004957, 17 pp. (2005).
- [221] A. Papayannis, D. Balis, P. Zanis, E. Galani, H. Wernli, C. Zerefos, A. Stohl, S. Eckhardt, V. Amiridis, *Annales Geophysicae* **23**, 2039 (2005).
- [222] T. Trickl, H. Feldmann, H.-J. Kanter, H. E. Scheel, M. Sprenger, A. Stohl, H. Wernli, *Atmos. Chem. Phys.* **10**, 499 (2010).
- [223] H. Jäger, *J. Geophys. Res.* **110**, D08106, doi: 10.1029/2004JD005506, 9 pp. (2005)
- [224] T. Deshler, R. Anderson-Sprecher, H. Jäger, J. Barnes, D. J. Hofmann, B. Clemensha, B., D. Simonich, R. Grainger, and S. Godin-Beekmann, *J. Geophys. Res.* **111**, D01201, doi: 10.1029/2005JD006608, 21 pp. (2006)
- [225] E. Danielsen, *J. Atmos. Sci.* **25**, 502 (1968).
- [226] M. Sprenger, M., Croci Maspoli, H. Wernli, Tropopause folds and cross-tropopause exchange: A global investigation based upon ECMWF analyses for the time period March 2000 to February 2001, *J. Geophys. Res.* **108**, 8518, doi: 10.1029/2002JD002587, STA 3, 11 pp. (2003).
- [227] G.-J. Roelofs, A. S. Kentarchos, T. Trickl, A. Stohl, W. J. Collins, R. A. Crowther, D. Hauglustaine, A. Klonecki, K. S. Law, M. G. Lawrence, R. von Kuhlmann, M. van Weele, Intercomparison of tropospheric ozone models: Ozone transport in a complex tropopause folding event, *J. Geophys. Res.* **108**, 8529, doi: 10.1029/2003JD003462, STA 14, 13 pp. (2003).
- [228] A. Stohl, P. Bonasoni, P. Cristofanelli, W. Collins, J. Feichter, A. Frank, C. Forster, E. Gerasopoulos, H. Gäggeler, P. James, T. Kentarchos, H. Kromp-Kolb, B. Krüger, C. Land, J. Meloen, A. Papayannis, A. Priller, P. Seibert, M. Sprenger, G. J. Roelofs, H. E. Scheel, C. Schnabel, P. Siegmund, L. Tobler, T. Trickl, H. Wernli, V. Wirth, P. Zanis, C. Zerefos, *J. Geophys. Res.* **108**, 8516, doi: 10.1029/2002JD002490,

- STA 1, 15 pp. (2003).
- [229] T. Trickl, H. Eisele, N. Bärtsch-Ritter, M. Furger, R. Mücke, A. Atmos. Chem. Phys. Discuss. **9**, 3113 (2009); a revised version was submitted for publication (2010).
- [230] O. Cooper, C. Forster, D. Parrish, E. Dunlea, G. Hübler, F. Fehsenfeld, J. Holloway, S. Oltmans, B. Johnson, A. Wimmers, L. Horowitz, J. Geophys. Res. **109**, D23S09, doi: 10.1029/2003JD004006, 18 pp. (2004).
- [231] M. A. Kritz, J.-C. Le Roulley, E. F. Danielsen, Tellus B **42**, 46 (1990).
- [232] D. Jaffe, T. Anderson, D. Covert, R. Kotschenruther, B. Trost, J. Danielson, W. Simpson, T. Berntsen, S. Karlsdottir, D. Blake, J. Harris, G. Carmichael, I. Uno, Geophys. Res. Lett. **26**, 711 (1999).
- [233] R. B. Husar, D. M. Tratt, B. A. Schichtel, S. R. Falke, F. Li, D. Jaffe, S. Gassó, T. Gill, N. S. Laulainen, F. Lu, M. C. Reheis, Y. Chun, D. Westphal, B. N. Holben, C. Gueymard, I. McKandry, N. Kuring, G. C. Feldmann, C. McClain, R. J. Frouin, J. Merrill, D. DuBois, F. Vignola, T. Urayama, S. Nickovic, W. E. Wilson, K. Sassen, N. Sugimoto, W. C. Malm, J. Geophys. Res. **106**, 18317 (2001).
- [234] O. Wild, J. K. Sundet, M. J. Prather, I. S. A. Isaksen, H. Akimoto, E. V. Browell, S. J. Oltmans, J. Geophys. Res. **108**, 8826, doi: 10.1029/2002JD003283, GTE 47, 10 pp. (2003).
- [235] Q. Liang, L. Jaeglé, R. C. Hudman, S. Turquety, D. J. Jacob, M. A. Avery, E. V. Browell, G. W. Sachse, D. R. Blake, W. Brune, X. Ren, R. C. Cohen, J. E. Dibb, A. Fried, H. Fuelberg, M. Porter, B. G. Heikes, G. Huey, H. B. Singh, P. O. Wennberg, J. Geophys. Res. **112**, 20 (2007), D12S11, doi: 10.1029/2006JD007919.
- [236] M. L. Büker, M. H. Hitchman, G. J. Tripoli, R. B. Pierce, E. V. Browell, J. A. Al-Saadi, J. Geophys. Res. **113**, D14S90, doi: 10.1029/2007JD009345, 14 pp. (2008).
- [237] H. Vömel, H. Selkirk, L. Miloshevich, J. Valverde-Canossa, J. Valdés, E. Kyrö, R. Kivi, W. Stolz, G. Peng, J. A. Diaz, J. Atmos. Oceanic Technol. **24**, 953 (2007).
- [238] B. Deuber, A. Haefele, D. G. Feist, L. Martin, N. Kämpfer, G. E. Nedoluha, V. Yushkov, S. Khaykin, R. Kivi, H. Vömel, J. Geophys. **110**, D13306, doi: 10.1029/2004JD005543, 10 pp. (2005).